2011

A Hierarchical Image Processing Approach for Diagnostic Analysis of Microcirculation Videos

Nazanin Mirshahi
Virginia Commonwealth University

Virginia Commonwealth University
Department of Computer Science

This is to certify that the dissertation prepared by Nazanin Mirshahi entitled A HIERARCHICAL IMAGE PROCESSING APPROACH FOR DIAGNOSTIC ANALYSIS OF MICROCIRCULATION VIDEOS has been approved by her committee as satisfactory completion of the Dissertation requirement for the degree of Doctor of Philosophy.

Kayvan Najarian, PhD, Advisor, Computer Science Department

Rosalyn S. Hobson, PhD, Co-Advisor, Electrical and Computer Engineering Department

---

Kevin R. Ward, MD, Emergency Medicine Department

Krzysztof J. Cios, PhD, Computer Science Department

Lorraine M. Parker, PhD, Computer Science Department

Todd C. Wittman, PhD, Mathematical Sciences Department

Date:

A HIERARCHICAL IMAGE PROCESSING APPROACH FOR DIAGNOSTIC ANALYSIS OF MICROCIRCULATION VIDEOS

A dissertation submitted in partial fulfillment of the requirements for the degree of Doctor of Philosophy at Virginia Commonwealth University.

by

NAZANIN MIRSHAHI

Advisor: KAYVAN NAJARIAN

Associate Professor, Computer Science Department

Virginia Commonwealth University

Richmond, VA

December, 2011

ACKNOWLEDGMENT

This work would not be possible without the support of my family, friends and advisors. First and foremost, my utmost gratitude to my aunts, Parvin and Giti, and my uncles, Sobhan and Aziz. They have been my guardians and given me love and support throughout this journey, far from my homeland. My beloved parents who always had faith in me and encouraged me, and my siblings, Nastaran and Shervin for inspiring me.

I am thankful to my advisor, Dr. Kayvan Najarian, who has given me the opportunity to work as a member of his group, and led me throughout the problems and uncertainties with his intelligence and knowledge. I am also thankful to my co-advisor, Dr. Rosalyn Hobson for her continuous support and kindness, and my friends in the lab for being wonderful.

Thanks.

Contents

List of Figures

List of Tables

ABSTRACT

A HIERARCHICAL IMAGE PROCESSING APPROACH FOR DIAGNOSTIC ANALYSIS OF MICROCIRCULATION VIDEOS

by Nazanin Mirshahi

A dissertation submitted in partial fulfillment of the requirements for the degree of Doctor of Philosophy at Virginia Commonwealth University.

Virginia Commonwealth University, 2011

Major Director: Kayvan Najarian, Ph.D.

Associate Professor, Virginia Commonwealth University

Knowledge of the microcirculatory system has added significant value to the analysis of tissue oxygenation and perfusion. While developments in videomicroscopy technology have enabled medical researchers and physicians to observe the microvascular system, the available software tools are limited in their capabilities to determine quantitative features of microcirculation, either automatically or accurately. In particular, microvessel density has been a critical diagnostic measure in evaluating disease progression and a prognostic indicator in various clinical conditions. As a result, automated analysis of the microcirculatory system can be substantially beneficial in various real-time and off-line therapeutic medical applications, such as optimization of resuscitation.

This study focuses on the development of an algorithm to automatically segment microvessels,

calculate the density of capillaries in microcirculatory videos, and determine the distribution of blood circulation. The proposed technique is divided into four major steps: video stabilization, video enhancement, segmentation and post-processing. The stabilization step estimates motion and corrects for the motion artifacts using an appropriate motion model. Video enhancement improves the visual quality of video frames through preprocessing, vessel enhancement and edge enhancement. The resulting frames are combined through an adjusted weighted median filter and the resulting frame is then thresholded using an entropic thresholding technique. Finally, a region growing technique is utilized to correct for the discontinuity of blood vessels. Using the final binary results, the most commonly used measure for the assessment of microcirculation, i.e. Functional Capillary Density (FCD), is calculated.

The designed technique is applied to video recordings of healthy and diseased human and animal samples obtained by MicroScan device based on Sidestream Dark Field (SDF) imaging modality. To validate the final results, the calculated FCD results are compared with the results obtained by blind detailed inspection of three medical experts, who have used AVA (Automated Vascular Analysis) semi-automated microcirculation analysis software. Since there is neither a fully automated accurate microcirculation analysis program, nor a publicly available annotated database of microcirculation videos, the results acquired by the experts are considered the gold standard. Bland-Altman plots show that there is "Good Agreement" between the results of the algorithm and that of gold standard.

In summary, the main objective of this study is to eliminate the need for human interaction to edit/ correct results, to improve the accuracy of stabilization and segmentation, and to reduce the overall computation time. The proposed methodology impacts the field of computer science through development of image processing techniques to discover the knowledge in grayscale video

frames. The broad impact of this work is to assist physicians, medical researchers and caregivers in making diagnostic and therapeutic decisions for microcirculatory abnormalities and in studying of the human microcirculation.

Chapter 1

Contributions and Novelty

The revolution in microcirculatory research occurred as a result of advances in tools for observing microcirculation. As clinical aspects of microcirculation have been developed by the researchers in medicine, other branches of science and engineering entered the field to facilitate clinical studies. While engineers have designed and created devices for microcirculatory studies, disciplines such as computer science provided tools for the analysis and assessment.

Acquiring microcirculation data is a rather uncomplicated process and can be performed for a large number of patients, but the technology is not widely used due to lack of efficient and accurate processing tools. The theoretical foundations of the proposed method are based on known computer science concepts. Several image processing and video processing theories have been studied to develop the proposed technique for analysis of microcirculation videos. The developed method is capable of calculating a quantitative measure of microcirculation, which allows for better understanding of the microcirculatory network in the sampled area. This study contributes to the field of microcirculation through mathematical methodologies in the field of computer science and helps in more extensive uses of the technology. The effective combination of relevant original and improved mathematical concepts have resulted in a technique to offset the shortcomings of the

existing microcirculation analysis techniques. The developed algorithm contributes to the field of computer science through development of novel concepts in image processing and knowledge discovery. Methods such as wavelet transform and contrast limited adaptive histogram equalization have been used in their original form, while the foundation of algorithms for vesselness filter, adjusted weighted median filter and entropic thresholding have been mathematically advanced through the proposed research to generate improved results. Furthermore, advancement in the utilized techniques has led to a superior way of knowledge discovery in the microcirculation data. Knowledge discovery is a concept in the field of computer science which deals with exploring a large volume of data through use of mathematically-based methods to find patterns in the data. Within the blue box Figure 1.1, knowledge discovery elements of the proposed method are outlined. The method enables processing of videos containing several frames, each frame comprised of several thousand pixels in a quick and accurate manner. The intensity value of each pixel is a number (e.g. belonging to [0 1], [0 255], etc.) which is modified through mathematical operations based on computer science concepts.

Numerous studies indicate that microcirculatory network features change in patients with severe heart conditions, sepsis, sickle cell, hypertension, diarrhea, diabetes as well as those in need of resuscitation [4, 5, 6, 7, 8]. Most patients with such diseases undergo a state called "shock". Shock is characterized by decrease in the delivery of oxygen and nutrients to tissues which is a direct effect of the changes in the functionality of microcirculation [9]. The treatment options depend on the type of shock including cardiogenic, septic, neurogenic and hemorrhagic shock; however, all such treatments require knowledge of the status of microcirculation in patients. For instance, in the case of resuscitation, the timing and the extent of resuscitory efforts need to be well-measured and well-controlled, otherwise the efforts might exacerbate the complication rather than being life-saving

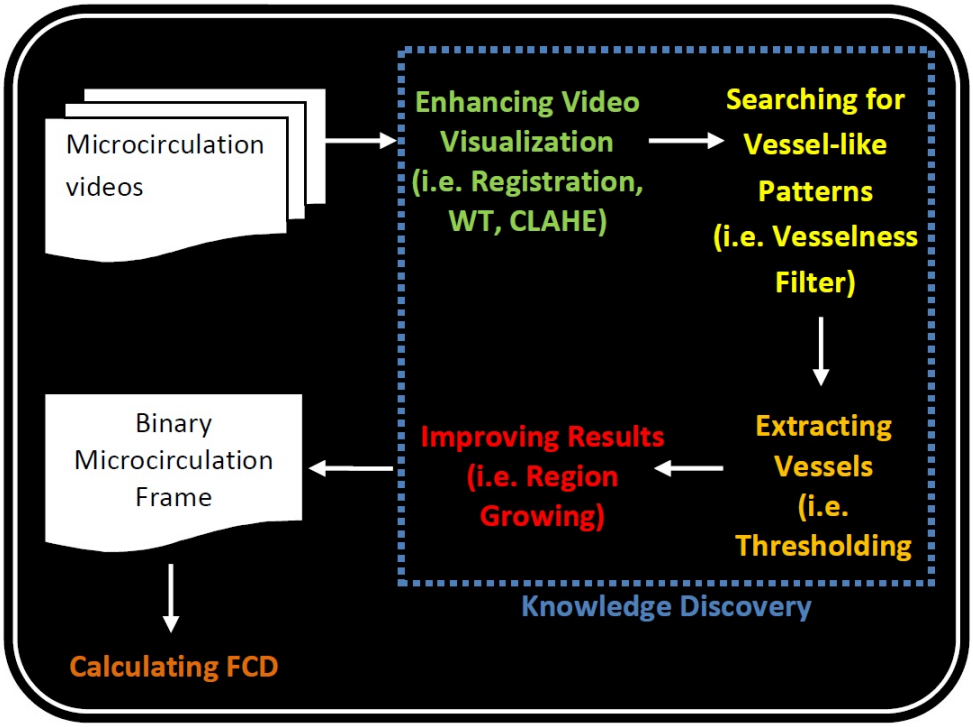

Figure 1.1: Knowledge Discovery framework

[10].

Accordingly, advances in techniques for analyzing microcirculation can assist medical caregivers in providing optimal level of service to a wide range of patients with the mentioned clinical conditions. This range includes cardiovascular diseases of various kind that each year affect the lives of approximately 81 million of Americans, according to the American Heart Association in 2010 [11]. Sudden cardiac death strikes 325,000 people in the United States every year [12]. In the United States, sepsis affects 750,000 patients annually, and sickle cell anemia affects 70,000 to 100,000 patients annually [13, 14]. According to 2011 health statistics, 68 million Americans suffer from hypertension [15].

Along with devices for capturing and monitoring microcirculation, advances in techniques for assessment of such data is critical to the field. While not intended to replace clinical caregivers,

software tools have an effective role as computer-assisted medical decision-making systems. The information being provided by such systems helps physicians monitor the status and changes in patients' physiology over the course of treatment. In addition, physicians would be capable of acquiring quantitative measures of microcirculation that are not perceived by human eyes and could improve diagnostic and treatment planning.

Following the innovation of advanced imaging modalities, software tools that enable users to assess microcirculation videos have been also developed. Meanwhile, the importance of software systems has been recognized by the widespread application of imaging systems. Consequently, the scope and complexity associated with the performance of software systems have increased. In the microcirculation field, the current commercially available software tools have had major improvements, yet none has completely addressed the outstanding need of a fully automated, close to real-time, accurate system. A fully automated system decreases human error and the burden of manual adjustments. A close to real-time system reduces the amount of time needed for generating quantitative results. This goal cannot be met unless the system is fully automated. Most clinical applications such as resuscitation are time sensitive and require immediate attention of caregivers. Generating highly accurate results is the goal of any decision-making system, since lack of sufficient accuracy may have adverse effects on the choice of proper treatment option.

The most popular commercially available software tools are CapImage, CapiScope and Advanced Vascular Analysis (AVA) [16]. CapImage performs quantitative estimation of red blood cell velocity, vessel diameter and vessel length, but its capability is limited since the user is required to manually draw the lines to select vessel segments and define the geometry. CapiScope is semi-automated and requires stable images. The most advanced software tool, AVA generates relatively accurate results, yet it is not fully automated. The proposed method is designed as a fully automated system that

receives microcirculation videos as input to generate highly accurate output. The novelty of the designed algorithm is as follows:

1. The algorithm introduces a novel thresholding technique for the segmentation of microcirculation video frames. Thresholding methods are commonly incorporated in image and video processing applications; however, none considers flow information in videos to be a factor for optimal thresholding. Experiments with microcirculation videos have shown that flow information can be considerably important in selecting an optimal threshold level. The proposed algorithm combines information regarding the intensity of each pixel and that of each pixel neighborhood intensity in a frame with the newly defined flow factor after video stabilization to determine the threshold level for each set of 20 consecutive video frames.

2. One major objective and achievement of this research is to identify small blood vessels and capillaries in each frame. An approach to determine whether an object in a frame is a small blood vessel/ capillary is proposed. The "vesselness" function used in this study is a modification of an earlier technique that works through modifying the effect of existing parameters in the "vesselness" equation. The proposed function reduces the effect of background noise while preserving the edges of diminutive capillaries. The original equation uses a combination of eigenvalues of Hessian in an image to characterize an object as a capillary or a non-capillary. In the proposed equation, two of the terms in the original equation are changed, while the remaining terms are kept unchanged.

3. Prior to segmentation, the results of the video enhancement step are combined using a novel method called Adjusted Weighted Median Filter (AWMF). The filter is an improved version of weighted median filtering that combines the intensity value of each pixel at a (x, y) coordinate

across 20 frames. The filter inserts a newly introduced Shift Index (SI) to the weighted median filtering equation. Shift index adds an effective bias term to the regular median filter to favor black pixels over white ones and vice versa.

Chapter 2

Background

Microcirculation refers to blood circulation in small capillaries with the diameter of less than 100 μm (too small to be observed with naked eye), and can be defined as a network that controls chemical and physical equilibrium required for the function of the tissue [17]. The microcirculatory system incorporates the delivery of oxygen, nutrients, hormones to target cellular components of the tissues. As a result, microcirculatory system can portray different types of microcirculation pathologies (angiopathies) in case of abnormalities. Accordingly, knowledge of the distribution and circulation of blood in capillaries can be a key indicator of human physiological health. The essential role of small blood vessels is further realized knowing that since the wall of large vessels tends to be thicker, the large blood vessels contribute less to oxygenation compared to small ones [18]. Due to complexity of humans and that of the topology of microcirculatory network, the microcirculatory science has been developed to describe different aspects of blood distribution in small blood vessels.

When flow changes in capillary network due to changes elsewhere in the circulatory system, the impediment to circulate in the capillaries also changes. Considering their small size, capillaries and small blood vessels characterize such alteration in blood circulation more evidently compared to large blood vessels. The significance of blood circulation in small blood vessels and capillaries lies

in the rheological properties of blood in microcirculation, particularly viscosity.

The pathology of microcirculation has been long studied by researchers in medical field. Changes in microcirculation may occur due to manifestation of diseases such as chronic ulcers, sickle cell, sepsis, diabetes mellitus and hypertension [4, 5, 6, 7, 8]. Diseases have different effects on microcirculation depending on their nature. Commonly, a disease converts a flowing capillary to a non-flowing one and this phenomenon alters the capillary network. For instance, in sepsis, microcirculatory dysfunction affects the distribution of microcirculation which might lead to organ failure/ dysfunction [3]. Microcirculation is called "the motor of sepsis" since microcirculatory abnormalities can define the severity of sepsis.

Development of hardware systems to observe such alterations has been a major step in microcirculatory science. Laser Doppler Flowmetry (LDF) is an early technology to assess blood circulation at a microscopic level, using a fluorescence microscope based on Doppler effect. In LDF, red light is emitted from a light source to a tissue. The flowmeter reads the frequency of the oscillation generated by Doppler frequency shift of the moving red blood cells in the tissue, and interprets that to an intensity oscillation. [19]. Figure 2.1 is an illustration of the principle of laser Doppler flowmetry. Despite being an effective research tool, LDF has been replaced by more reliable techniques. The two most used imaging modalities in the field of clinical microcirculatory research, in particular for in vivo visualization of microcirculation, are Orthogonal Polarization Spectral (OPS) imaging and Side-stream Dark Field (SDF) [20, 21]. The two techniques are capable of producing high resolution images of microcirculation.

OPS utilizes polarized green light with a wavelength of 550 nanometer that is received by erythrocytes. The reflection of the light has a 90° angle to the emitted light, and is measured

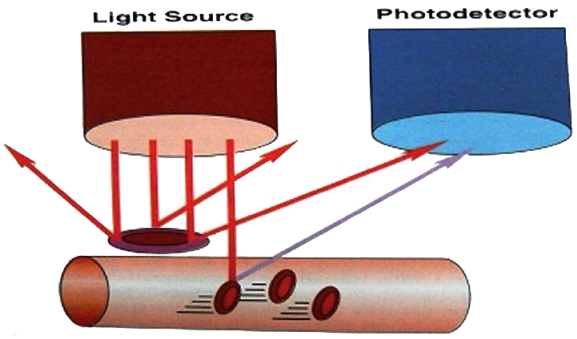

Figure 2.1: Principle of laser Doppler flowmetry [1]

after the polarized portion was filtered out. The measurement characterizes the image of the tissue that received the light. In other words, OPS produces the image by using sub-surface scattering of polarized light, which appears as if there is a virtual source of light within the tissue. The technique is well-developed and provides high resolution, high contrast medical images that are widely used in clinical and research settings. Figure 2.2 illustrates OPS modality [22].

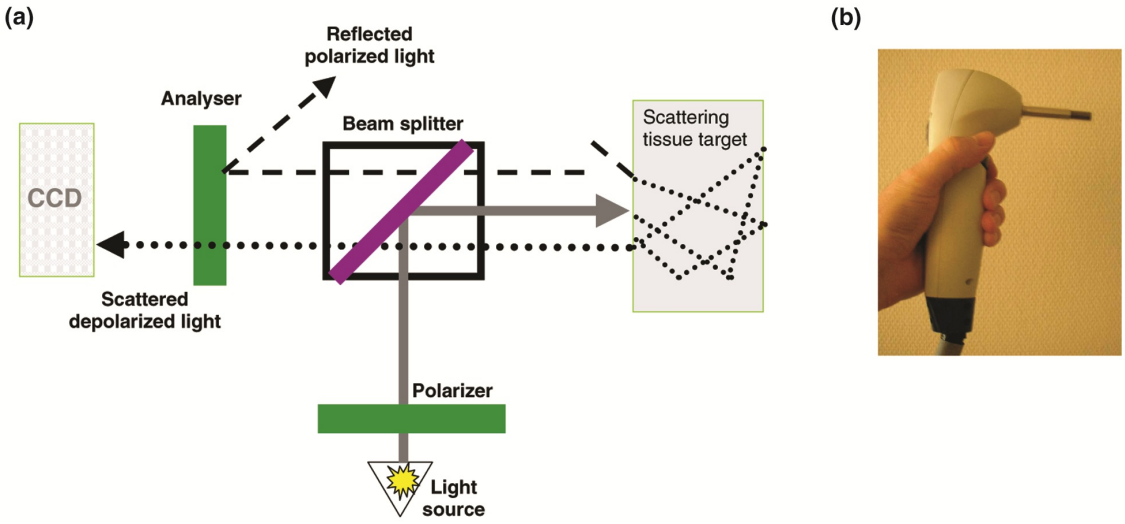

Figure 2.2: (a) Orthogonal polarization spectral imaging technique (b) built into a simple hand-held device [2]

SDF has been introduced after OPS to address the shortcoming of OPS, which is sensitivity to internal scatter of light. This drawback of OPS results in blurring especially in microcirculation

images. In SDF modality, Light Emitting Diodes (LED) transmit light with a wavelength of 530 nanometer. The hemoglobin of erythrocytes absorbs the light, so to be visualized as flowing cells. SDF does not cause blurring and produces clear images of capillaries. Consequently, the analysis of the captured images becomes less complicated. A demonstration of SDF mechanism of action is presented in Figure 2.3.

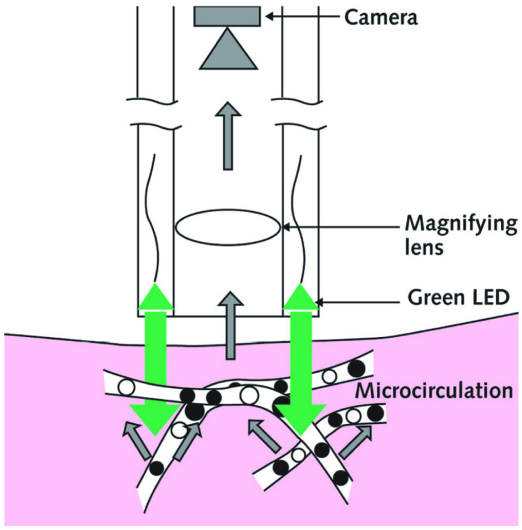

Figure 2.3: Side-stream Dark Field technique [3]

One imaging instrument to capture the SDF videos is called MicroScan Video Microscope System produced by MicroVisionMedical [16]. The instrument consists of an imaging unit, a battery unit, a detachable handle, a calibration unit, sterile disposable lenses, and a connecting cable to an A/C adapter with power plug. To capture the data in this study, the device is held by the handle, and the tip of the imaging unit is gently placed on sublingual surface. The hemoglobin in Red Blood Cells (RBCs) reflects the LED illumination from the imaging unit, which makes the wall of vessels visible [20]. An illustration of the imaging device and recording of microcirculation video of the sublingual surface from a subject are shown in Figure 2.4 and Figure 2.5.

The acquired videos with either OPS or SDF imaging modalities require effective analysis in or-

Figure 2.4: MicroScan Video Microscope System produced by MicroVisionMedical

Figure 2.5: Recording microcirculation video of the sublingual surface from a subject using MicroVision system

der to be used in clinical settings. The image processing techniques used for blood vessel extraction can be divided into five major categories:

1. Staal et al. have introduced pattern recognition-based methods to analyze 2-dimensional retina images [23]. Pattern recognition techniques deal with identifying features and classify them in order to extract relevant useful information depending on the application. This class of techniques cannot be effectively used for microcirculation images due to low resolution, low local contrast of the images and wide variety of patterns.

2. Tracking-based approach locates a landmark (e.g. in case of retinal images, the optic nerve in ocular fundus images), and uses features such as convergence of vessel network and brightness to segment the blood vessels [24]. Tracking-based approach is unable to precisely detect blood vessels in the presence of bright lesion bubbles.

3. Model-based technique combines Laplacian, thresholding and classification methodologies to extract blood vessels [25]. Despite its strength in applications such as retinal image segmentation, the technique requires high level of human intervention.

4. Artificial intelligence-based techniques use prior knowledge about input to derive knowledge about output. The knowledge can be acquired from various sources and in different forms (e.g rules describing the properties of an object or the relation between the objects)[26].

5. Neural network-based techniques find pattern in data and classify input data into different classes. This class of techniques does not extract vessel structures; however, it can be trained with annotated input images to detect vessel objects from non-vessel objects.

The proposed method in this research is a hierarchical combination of video processing and image processing concepts. Reviews of closely related work to the specific video and image processing techniques utilized in the proposed methodology is presented in the following subsections.

2.1 Related Work for Vessel Enhancement

Vessel enhancement is comprised of a set of filters and operations to improve the visualization and quantitative analysis of blood vessels. Various approaches to enhance vascular structures exist in literature. One class of techniques, which applied at a single fixed scale, performs a combination of difference operators to enhance the structure of vessel-like objects in images such as magnetic resonance angiography [27, 28]. This class of methods is unable to detect vessels of different sizes since it only operates over a fixed scale.

The class of multi-scale approaches to vessel enhancement is comprised of cores, steerable

filters, along with ways for the analysis of local orientation of shapes through assessment of eigenvalue of the Hessian matrix [29, 30, 31, 32]. The proposed vessel enhancement technique in this study belongs to the multi-scale class. The eigensystem of the Hessian can be used for geometrical interpretation of vessel-like structures. The foundation of the proposed technique was first developed by Sato et al. and Lorenz et al., then further expanded by Frangi et al. [31, 32, 33].

Techniques based on Vessel Enhancing Diffusion (VED) use diffusion schemes including isotropic diffusion scheme, small diffusion for non-vessel structures scheme, and minimal principal curvature direction of the isosurface scheme [34, 35, 36]. In this class, a structure-preserving diffusion tensor is defined in diffusion equation of the filter. Most of the techniques in this class have been designed and extended for 3-dimensional structures.

2.2 Related Work for Edge Enhancement

Edges are characterized by local changes or discontinuities in image luminance [37]. Edge detection techniques consist of a series of operations to improve the visualization of image boundaries (e.g. vessel boundaries). Edge detection techniques can be categorized into two main groups: edge enhancement techniques and edge fitting techniques. In the edge enhancement class, neighborhood operators are used to detect the discontinuities in the graylevel intensity of the image. Methods in this category include Robert's, Prewitt and Sobel operators in which convolutional kernels of various sizes are used, along with Laplacian and Difference of Gaussian (DoG) filter. In DoG filter, derivatives of different orders are used to detect edges. The method used for edge enhancement is kernel-based which detects line segments (vessel pattern) in microcirculation images.

The edge fitting class minimizes the distance between the original image and a mask which is a predefined edge model. One method in this category was proposed by Hueckel in which the original image and the mask are represented in the form of vectors of coefficients; the method uses Fourier series to find orthogonal components. Other methods are based on projecting the image onto a set of functions in Hilbert space, or in the forms of energy/ wave functions. Another set of models are based on minimization of Least Mean Square (LMS) estimation errors, splines and Discrete Cosine Transform (DCT), which were proposed to model edge structure in the image locally and globally.

2.3 Related Work for Video Stabilization

Video stabilization is referred to a set of processes performed with the aim of reducing the motion between video frames. The ideal outcome of video processing is a new video in which the unwanted motion has been effectively eliminated. Video stabilization techniques can be divided into three main categories of mechanical stabilization, optical stabilization and digital stabilization [38]. The class of mechanical stabilization techniques uses mechanical devices such as tripods to hold the camera stable. The optical stabilization class adjusts the optical system using sensors to detect motion. The mentioned stabilization methods deal with video capturing device and cannot be used after recording the videos [39]. However, digital stabilization is a software-based approach that can be applied both while capturing the videos and after video capture.

The class of digital image stabilization can be divided into motion estimation and motion correction [40]. For motion estimation, the global motion vectors are calculated and then the unwanted motion is removed using the results of these calculations. Motion can be

2-dimensional, corresponding to only translation, or 3-dimensional corresponding to rotation-zoom transformation and translation [39, 41].

Motion estimation techniques can be also divided into two groups: region matching techniques and spatio-temporal constraint techniques [42]. Region matching methods include bit-plane matching, feature tracking, pyramidal approaches and block matching algorithms [40, 43, 39]. Spatio-temporal methods include direct optical flow estimation, phase correlation, integral projection and least mean-square error matrix inversion set of techniques [44, 41, 45, 46]. Spatio-temporal methods are less computationally expensive than region matching techniques.

The motion models can be divided into three categories [47]; Fully parametric, quasi-parametric, and non-parametric. Fully parametric models describe the motion of pixels in a given region in a parametric form. Quasi-parametric models describe motion of pixels in a parametric form over a specific region, while defining separate pixel to pixel local components. Non-parametric models utilize a variation of smoothness or uniformity constraint. The motion model used in this research is a quasi-parametric algorithm.

2.4 Related Work for Segmentation

Image segmentation deals with clustering an image into various segments/ regions depending on the particular application. The main objective of image segmentation is to convert the image into a form that is more meaningful and easier to analyze for humans or user systems.

Thresholding is the simplest method of image segmentation in which one or multiple threshold values are chosen to partition the image into different segments. Different thresholding techniques have been developed for a variety of image processing applications. The methods are divided into six main categories: Histogram shape-based thresholding methods examine the

shape properties of the histogram. Different aspects of the histogram such as the distance of convex hull and peak-and-valley can be factors for choosing the threshold value. In clustering-based thresholding methods, the graylevel pixel values are clustered into two clusters, which correspond to the two lobes of a histogram. The two clusters can be selected based on Gaussian mixture model, minimization of the weighted sum of within class variances of foreground and background, minimization of misclassification error, and Euclidean distance between a pixel value and the class mean. Thresholding based on object attribute uses some similarity measures between the original image and the binary image for thresholding. The similarity measures can be in form of edge matching, shape compactness, gray-level moments, connectivity, texture, or stability of segmented objects. Spatial thresholding uses a combination of graylevel distribution and the neighborhood information to choose the optimal threshold level. The neighborhood information can be presented in form of context probabilities, correlation functions, co-occurrence probabilities, and local linear dependence models of pixels. In a locally adaptive thresholding class of techniques, a threshold is calculated at each pixel based on local statistics such as range and variance. Entropy-based thresholding methods are based on maximizing the entropy of the graylevel histogram of the image. The maximum entropy corresponds to the maximum information transfer; therefore, the threshold value that is chosen based on the highest entropy value results in the lowest loss of information when converting the original image to the binary image. The proposed method used in this study can also be categorized in the entropy-based thresholding class.

Chapter 3

Proposed Method

This chapter introduces the proposed hierarchical video and image processing algorithm for detection of active capillaries in microcirculation videos. The proposed method is applied to videos captured with MicroScan system with Sidestream Dark Field (SDF) imaging modality; however, it can be applied to any type of microcirculatory videos. Data for this study has been captured from sublingual surface of healthy and diseased human and swine subjects. The samples have been acquired by experts at the School of Medicine of Virginia Commonwealth University and Virginia Commonwealth University Reanimation Engineering Science Center (VCURES).

The proposed algorithm receives a microcirculation video, consisting of a set of N video frames and divides it into sets of 21 frames. The grayscale intensity of the frames are in the range of 0 to 255. The final output of processing is a binary image in which capillaries are shown by black pixels and the background is shown by white pixels with intensity values of 0 and 1 respectively. The microcirculatory measure of Functional Capillary Density (FCD) is calculated using this binary image. Figure 3.1 illustrates the methodology. The purpose of applying the algorithm to sets of 21 consecutive frames in a video is to show the dynamics/

movement in capillaries. The major steps of the technique are as follows: video stabilization, video enhancement, segmentation and post-processing.

(a) Video stabilization: The original video frames need to be stabilized prior to being processed; therefore, in the sequence of frames, the best representation of motion that aligns pixels from one frame to the next one is chosen. The representation is described in the form of a motion model. The hierarchical method used for stabilization is a combination of a global model to define the estimated motion, a local model to set the requirements of the process, and a coarse-fine reinforcement framework. This process registers each video frame to the previous frame and results in reduction of unwanted motion artifacts.

(b) Video enhancement: The intensity values of capillaries and small blood vessels are close to that of background in the input microcirculation videos. Video enhancement is comprised of two parts: preprocessing and vessel enhancement. Preprocessing is a combination of techniques to correct for the low local contrast of microcirculation frames and to remove the effect of background noise. Wavelet transform and contrast limited adaptive histogram equalization are the approaches used for preprocessing. A vessel enhancement technique is applied to the preprocessed video frames to analyze the structure of the objects in each frame in order to better detect vessel-like objects. Finally, an edge enhancement algorithm is applied to strengthen the edges of the vessels.

(c) Segmentation: In the segmentation part, an adjusted weighted median filter is applied to each pixel coordinate across 20 consecutive frames to combine them into a single frame. Following that, an optimal threshold value is calculated, employing an entropic-thresholding technique. The technique uses the probability information of pixel intensity, intensity difference among neighboring pixels and a newly defined flow parameter to ob-

tain a threshold level for segmentation. The result of AWMF is then segmented to regions representing capillaries and background using the threshold value. The segmentation result is a binary image in which capillaries are in black and background is in white pixels.

(d) Post-processing: This step improves the results of the thresholding through growing the vessel regions and background regions. The region growing technique uses the intensity values of the gradient image and that of the result of AWMF to solve the issue of vessel discontinuity. Finally, functional capillary density (the area of capillaries/the area of the image) is computed for the resulting binary image.

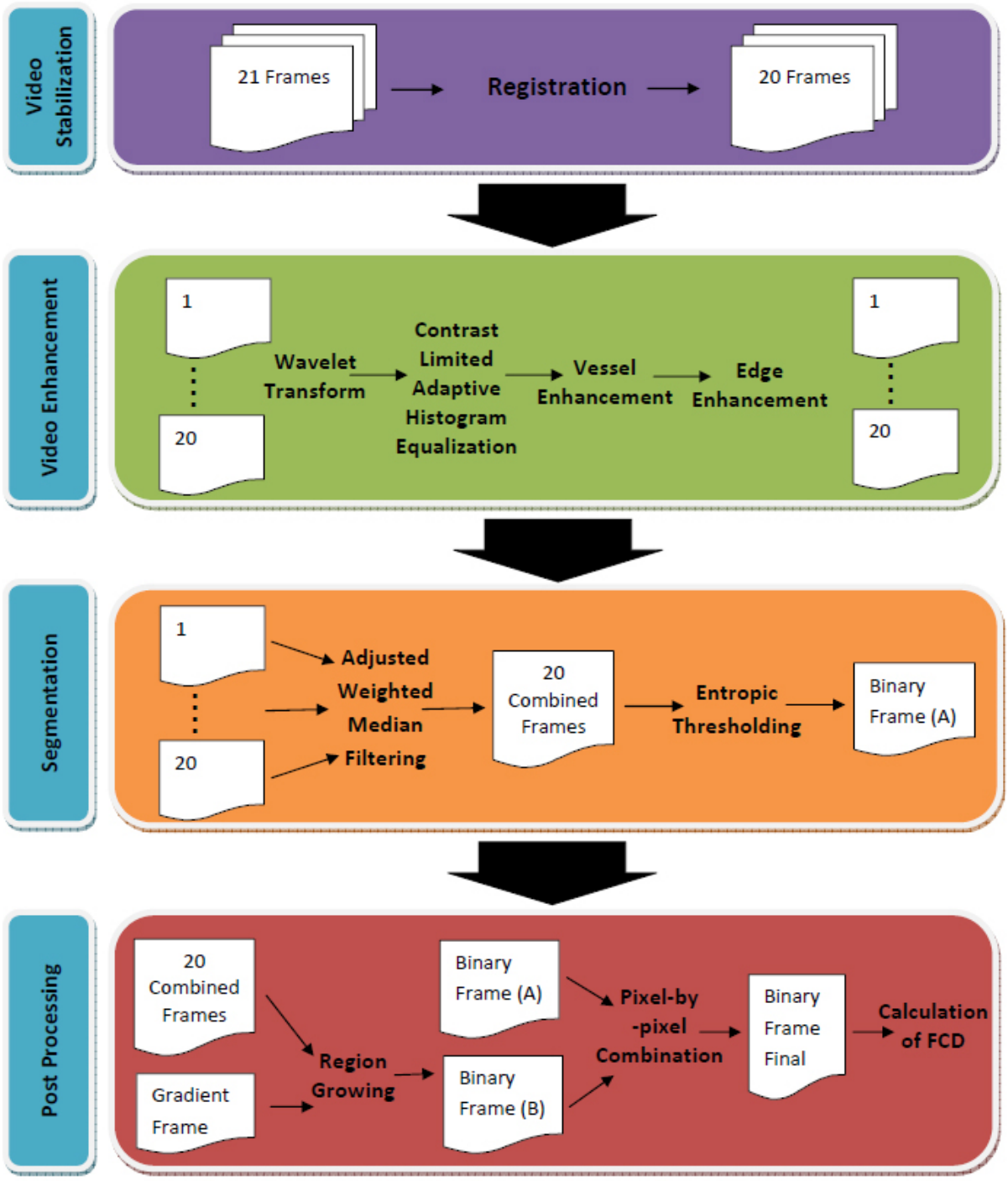

Figure 3.1: Diagram of the proposed methodology

Chapter 4

Video Stabilization

4.1 Overview

In this chapter, the steps to stabilize microcirculation videos are discussed. To stabilize frames, a hierarchical technique for motion estimation and correction to remove the effect of unwanted vibrations in the video sequences is used. The stabilization registers each pair of consecutive frames and prepares the video for further processing.

4.2 Description of the Method

Video stabilization is a key step in detecting and removing undesirable motion between consecutive frames. Videos are stabilized in order to eliminate any motion artifact caused by the movement of the subject or the vibration of the handheld camera, while preserving the motion of blood in the blood vessels. The stabilization algorithm receives 21 video frames as input, registers each frame to the preceding one, and generates 20 registered frames as output. Figure 4.1 presents the steps of the proposed techniques in this section.

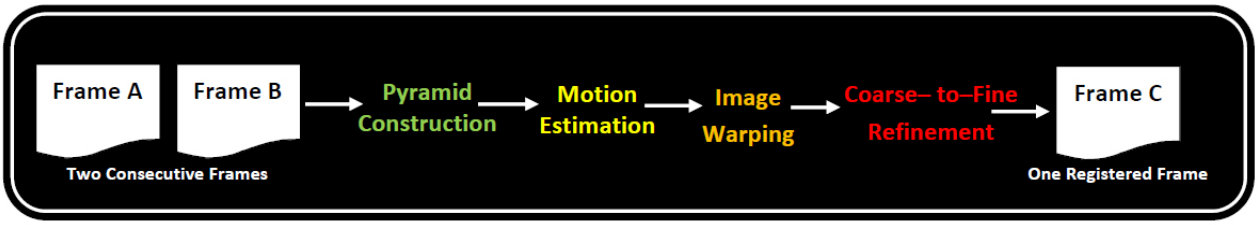

Figure 4.1: Diagram of the proposed video stabilization technique

4.2.1 Video Stabilization

Advances in video microscopy technology in the field of microcirculation have provided the tools for researchers to observe blood circulation. The main reason for recording videos of microcirculation is to capture sequence of frames and to be able to observe/ measure the blood flow in microvessels. In order to do so, video acquisition has to be perfect; i.e. no motion artifact is desirable in recorded videos. In spite of all the efforts to perfect the process of capturing videos, preventing undesirable movement of the cameras when dealing with human operators and human subjects has remained a challenge. Therefore, removal of the unwanted movement is essential for precise analysis of the videos. In this study, the unwanted movements do not have any effect on the content of an individual frame, but they cause shift in a single image compared to the previous one.

In order to track the shift in the contents of two consecutive frames, the implemented method recognizes the motion and registers images, distinguishing frame motion and blood motion in the frames [47]. The method consists of four key steps:

(a) Pyramid construction: The image pyramid refers to decomposition of the original image into a hierarchy of images at different scales (i.e. frequencies). The type of image pyramid built for this study is a Laplacian pyramid which is made using the difference

of levels in the corresponding Gaussian pyramid. To construct the first level of the Gaussian Pyramid, an image is filtered with a low-pass filter and then sub-sampled. The low-pass filter creates an equivalent effect as convolving the image with a series of Gaussian-like weighting functions followed by sub-sampling. In each level, also called iteration, the same procedure is repeated using the resulting image from the earlier step as the input image. The operation is the convolution of Gaussian blur kernel and the image, which eliminates high frequencies from the image. The pyramid compresses the image by making it coarser at each level and by reducing the number of bits of precision. Figure 4.2 illustrates four levels of a Laplacian pyramid for an original microcirculation frame.

(b) Motion estimation: The choice of motion model for the motion estimator depends on the type of input, however all motion estimator models minimize Sum of Squared Differences (SSD). The main assumption for the minimization is the constancy of intensity which is formulated in Equation 4.1:

$$I(X,t) = I(X - u(X), t - l) \tag{4.1}$$

where $X = (x, y)$ is the position of a point, I is the image intensity, and $u(X) = (l(x,y), v(x,y))$ which is the image velocity at point (x, y). The SSD is calculated as follows:

$$E(\{u\}) = \sum_{X} (I(X,t) - I(X - u(X), t - l))^2 \tag{4.2}$$

where $\sum_X$ is calculated for the points within the region and $\{u\}$ is the flow field within the region. The general form of the motion model is described in Equation 4.3:

$$u(X) = u(X; P_m) \tag{4.3}$$

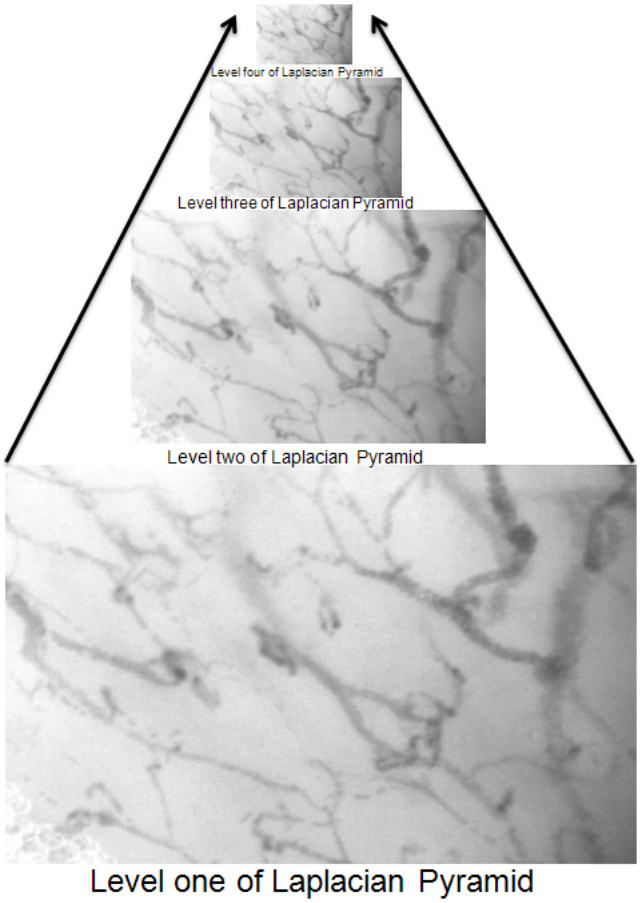

Figure 4.2: Representation of four levels of the Laplacian pyramid for an original microcirculation frame

where P_m is the vector for model parameters. As can be seen in Equation 4.3, the general form of the problem is independent from the choice of motion model. To solve the problem of calculating sum of squared errors, the Gauss-Newton method is used. The Gauss-Newton method utilizes the first order expansion of the error values prior to squaring.

Consider $\{u\}_i$ to be the estimate of flow field at the ith iteration and $\{\delta u\}$ to be the incremental estimate. The error measure is computed as follows:

$$E(\{\delta u\}) = \sum_X (\Delta I + \nabla I.\delta u(X))^2 \tag{4.4}$$

where the difference of the intensity value of a pixel in two consecutive frames is calculated with Equation 4.5:

$$\Delta I(X) = I(X,t) - I(X - u_i(X), t-1) \tag{4.5}$$

Equation 4.4 shows the general form of motion problem which is an under-constrained equation. Any particular type of motion constrains the equation in a different manner. The particular type of motion selected for microcirculation video frames is rigid body, which cannot be modeled by a single global model. Therefore, combination of a global and local models is used to describe the motion. The rigid motion can be formulated as follows:

$$u(x) = \frac{1}{Z(X)} A(x)t + B(x)\omega \tag{4.6}$$

where x is the image position and $Z(X)$ is the depth of the image. $A(x)$ and $B(x)$ are the following matrices:

$$A(x) = \begin{bmatrix} -f & 0 & x \\ 0 & -f & y \end{bmatrix} \tag{4.7}$$

$$B(x) = \begin{bmatrix} \frac{(xy)}{f} & \frac{-(f^2+x^2)}{f} & y \\ \frac{(f^2+x^2)}{f} & \frac{-(xy)}{f} & -x \end{bmatrix} \tag{4.8}$$

The local model used is frontal planar which assumes that $Z(X)$ is constant. During multiple iterations, the parameters of global model ω and t and that of local model $Z(x)$ are refined.

The estimation algorithm begins with initial values of $Z_i(X)$, t_i, ω_i and $u_i(X)$. $u_i(X)$ is used for warping the original image towards the following one. The estimated error between the original image and the warped image is used for updating the parameters

of local and global models. Using this, Equation 4.6 can be rewritten as follows:

$$\delta u(x) = \frac{1}{Z(X)} A(x)t + B(x)\omega - \frac{1}{Z_0(X)} A(x)t_0 + B(x)\omega_0 \tag{4.9}$$

Using that, Equation 4.4 can be rewritten as follows:

$$E(t, \omega, \frac{1}{Z(X)}) = \sum_X (\Delta I + (\nabla I)^T At/Z(X) + (\nabla I)^T B\omega - (\nabla I)^T At_i/Z_i(X) - (\nabla I)^T B\omega_i)^2 \tag{4.10}$$

For this study, it is assumed that $\frac{1}{Z(X)}$ is constant over windows of size 5×5 pixels. Equation 4.10 is differentiated with respect to $\frac{1}{Z(X)}$ and set to zero in order to obtain the value of $Z(X)$. Using $\frac{1}{Z(X)}$, global estimation of errors (E_{global}) and local estimation of error (E_{local}) can be calculated with Equation 4.11 and Equation 4.12.

$$E_{local} = \sum_{5\times5} E(t, \omega, \frac{1}{Z(X)}) \tag{4.11}$$

$$E_{global} = \sum_{image} E(t, \omega, \frac{1}{Z(X)}) \tag{4.12}$$

The values of ω and t are refined in each iteration through the Gauss-Newton minimization of the values of ω and t in the previous iteration.

(c) Image warping: The technique uses the current values of the parameters of the model to calculate the flow field. Using the flow field, the warping algorithm uses flow field to warp $I(t-1)$ towards $I(t)$. Bilinear interpolation is used for this purpose. ΔI is calculated using the warped image in each estimation, while ∇I is calculated using the reference image.

(d) Refinement: The refinement process updates the parameters of motion model as the algorithm finishes each level. For microcirculation images, four levels of the Laplacian pyramid are generated and each level is refined four times. The refinement process starts

with the coarser (image at level four of the pyramid) and ends with the finest (image at level one of the pyramid).

Figure 4.3 shows the first, 10th and 20th registered subfigures of a set of 20 registered frames, respectively. One bifurcated blood vessel is selected in a blue window for better tracking of the intensity changes. The intensity changes are due to blood circulation. As a result of registration, the motion artifacts are reduced in order to better observe the blood flow.

Following registration, the pixel-wise distance/ difference between the intensity values of each pair of consecutive frames is calculated. The calculated distance is used in the segmentation section to compute "flow parameter".

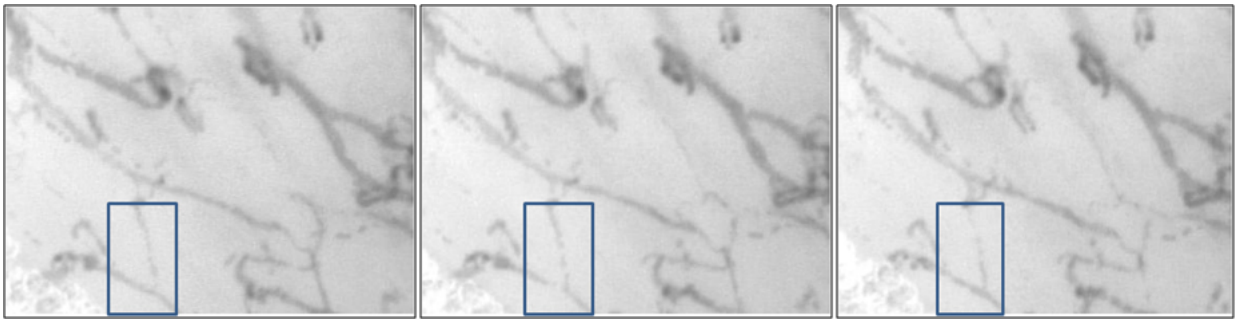

Figure 4.3: From left to right, frame 1, 10 and 20 of a set of 20 registered frames. The blue rectangle is used to better track the changes in one bifurcated blood vessel

Chapter 5

Video Enhancement

5.1 Overview

This chapter provides a detailed description of the methodology for the visualization enhancement of microcirculation videos. The captured microcirculation videos have low local contrast, which complicates the processing of video frames. Video enhancement consists of three steps of preprocessing, vessel enhancement and edge enhancement techniques, which are discussed in this section. Figure 5.1 illustrates the proposed techniques.

Figure 5.1: Diagram of the proposed video enhancement technique

5.2 Description of the Method

Video enhancement modifies the intensity values of the pixels in the image, enabling greater visualization of the pixels belonging to background and the ones belonging to the objects. The enhancement begins with de-noising through wavelet transform and contrast improvement

through contrast limited adaptive histogram equalization. The two mentioned operations improve the image grayscale intensity. Further operations are performed to detect vessel-like objects and enhance the identification of the vessels through vessel enhancement and edge enhancement respectively.

5.2.1 Preprocessing

The algorithm begins by converting a microcirculation video into its comprising frames. The video recording device used in this study captures 29 frames per second. A microcirculation frame is a single microcirculation image that contains background and foreground. The foreground consists of capillaries, small blood vessels as well as large blood vessels, and the background is the remaining part of the image. Preprocessing consists of a set of steps to improve the visual quality of the image, to reduce blurring and noise, to enhance the contrast and to reveal more details about image.

In the first step of preprocessing, 2-dimensional wavelet transform is applied to the video frames to filter the high frequency noise. Discrete wavelet transform is a classical effective technique for image de-noising [48]. The transform produces an image representation with better spatial and spectral localization of image formation, compared to other representations such as the Gaussian pyramid. It decomposes the original image into an approximation coefficient image and three detail coefficients images at each level of decomposition. Figure 5.2 illustrates the hierarchical structure of discrete wavelet transform in the first and second level of decomposition. The 2-dimensional array of coefficients ($a_{j,k}$) are calculated using Equation 5.1. The decomposition function is applied separately to each row and each column

of the image $f(t)$.

$$a_{j,k} = \sum f(t)\psi^*_{j,k}(t) \tag{5.1}$$

Where ψ is the wavelet function:

$$\psi^*_{j,k}(t) = \sqrt{2^{-j}}\psi(2^{-j}t - k) \quad j,k \in Z \tag{5.2}$$

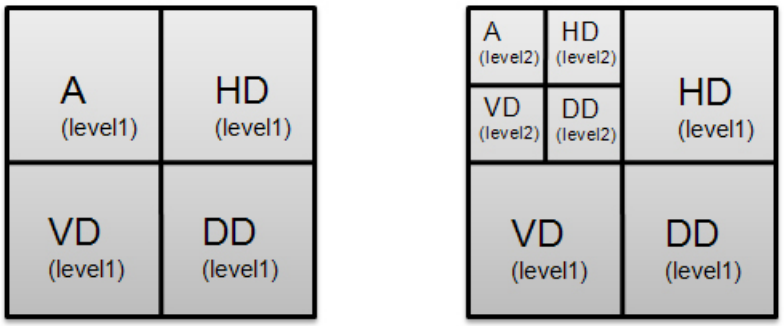

Figure 5.2: Hierarchical structure of discrete wavelet transform, Level 1 and level 2. (A: Approximation, HD: Horizontal Details, VD: Vertical Details, DD: Diagonal Details)

In practice, an appropriate mother wavelet replaces the wavelet function. The choice of mother wavelet depends on the particular application. Although the proper choice of mother wavelet is crucial to the performance of de-noising, the common way of choosing a mother wavelet is trial and error. For this application, a number of mother wavelets were examined to find the most appropriate match to the original image. Mother wavelet of form Daubechies 8 was selected through multiple testing and visual inspection of the results. Furthermore, testing the output of several levels of decomposition on the data has shown that level 2 leads to an optimal result. As the levels of decompositions go up, the decomposed images become smaller and coarser. In the decomposed image, high frequency components are set to zero and the remaining components are reconstructed to form the resulting image. In order to

reconstruct the image, the transformation needs to be inversed using Equation 5.3:

$$f(t) = \sum_{k} \sum_{j} a_{j,k}\, \psi_{j,k}\,(t) \tag{5.3}$$

Inverse wavelet transform reconstructs the image with the same mother wavelet after the removal of diagonal details coefficients. The resulting reconstructed image contains less noise than the input image.

The next step in preprocessing is local contrast enhancement to improve the visual quality of the video frames. The existing medical imaging modalities cover a large range of contrast information. For instance, SDF images spread over a grayscale range from 0 to 255; however, the human visual system is only capable of perceiving 100 different grayscale intensities [49].

The preprocessing algorithm applies a customized version of the Contrast Limited Adaptive Histogram Equalization (CLAHE) to the output of wavelet transform [50]. Used for improving poor or excessive lighting conditions, global contrast enhancement techniques are not applicable in the case of microcirculation images. CLAHE enhances local contrast of the objects by modifying the intensity value of pixels in a frame. CLAHE operates locally and divides the image into small regions known as 'tiles'. The histogram of each tile, which shows the number of pixels at each intensity level in the tile, is calculated. The histogram is adjusted in each tile to enhance the contrast of each region. The distribution of the desired histogram shape is specified and the contrast is altered so to match the distribution. The result is an image divided into windows of enhanced sub-images. A problem with the resulting image is that the borders of the windows are very evident. To obtain a uniform image, the adjacent tiles are smoothed out through bilinear interpolation. Bilinear interpolation incorporates the values of the four closest pixels surrounding a pixel in the original image to calculate the new value

of that pixel in the output image. The value of the interpolated pixel is a weighted average of pixels in the nearest 2×2 neighborhood of a pixel and is obtained through fitting the simplest surface to the four points. The interpolation reduces the effect of the tile boundaries and makes the entire frame look more homogeneous.

The number of tiles determines the size of the regions. The optimal number of tiles can vary depending on the input image. For the microcirculation frames of this study, tiles of size 10×10 pixels were chosen through experiment. Considering that the size of the largest acceptable capillary is 10 pixels, smaller windows may only show part of a capillary, while larger windows may not be sufficiently effective for contrast improvement. To control the adjustment of contrast, a contrast factor called Clip-Limit is defined to limit the contrast enhancement. Clip-Limit controls the number of pixels in the same intensity range. This factor prevents over-saturation in the image. The function for the transform of image contrast to the desired contrast is specified by a distribution. The histogram shape for the tiles is set to 'rayleigh' with the following equation, defined for x values [51]:

$$f(x, \sigma) = \frac{x}{\sigma^2} e^{\frac{-x^2}{2\sigma^2}}, \ x \geq 0 \tag{5.4}$$

Where σ is the parameter of the distribution and given the integer value of 2 for this experiment. The combination of Clip-Limit and contrast transform function controls the amount of change in the image contrast.

The contrast of the image is increased as a result of employing the customized variation of CLAHE, hence the distinction between objects and background becomes clearer. An original microcirculation video frame is shown in Figure 5.3. The result of applying preprocessing to that frame is shown in Figure 5.4. The shape of the histograms of Figure 5.3 and Figure

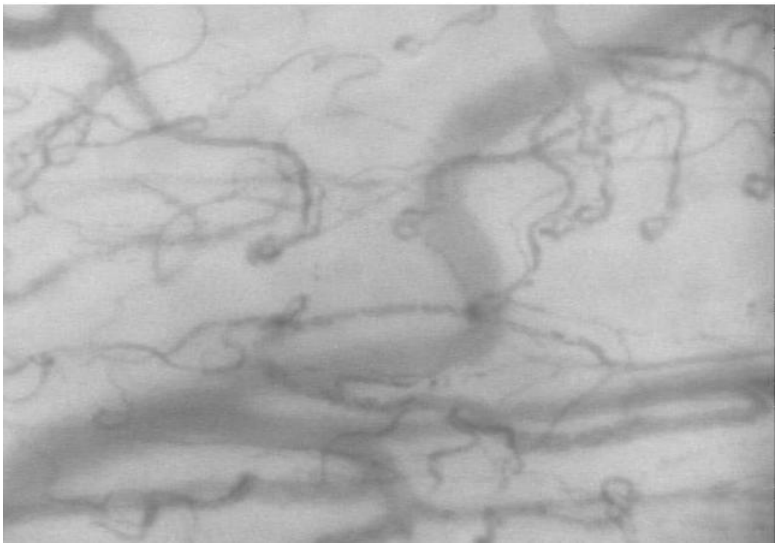

Figure 5.3: Original microcirculatory video frame of a subject

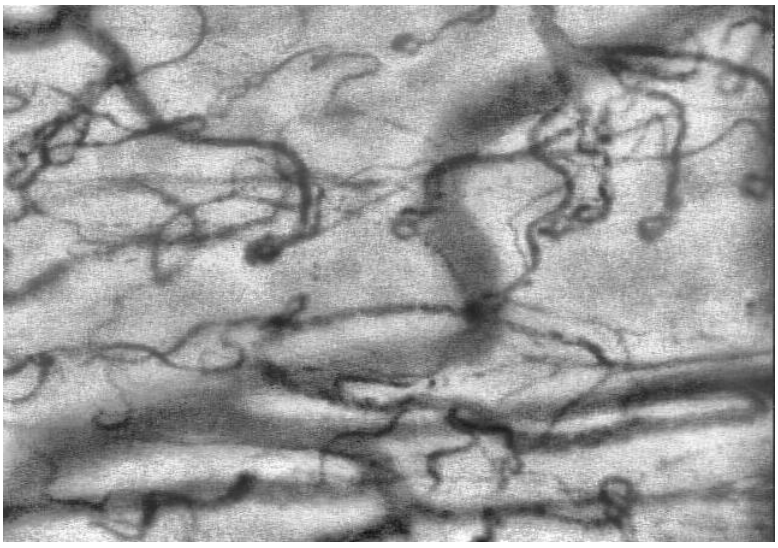

Figure 5.4: Result of preprocessing of Figure 5.3

5.4 are shown in Figure 5.5. While in the histogram of the original frame only one peak is evident, in the histogram of the preprocessed frame two distinct peaks, one belonging to the objects and the other belonging to the background the histogram after preprocessing, can be seen.

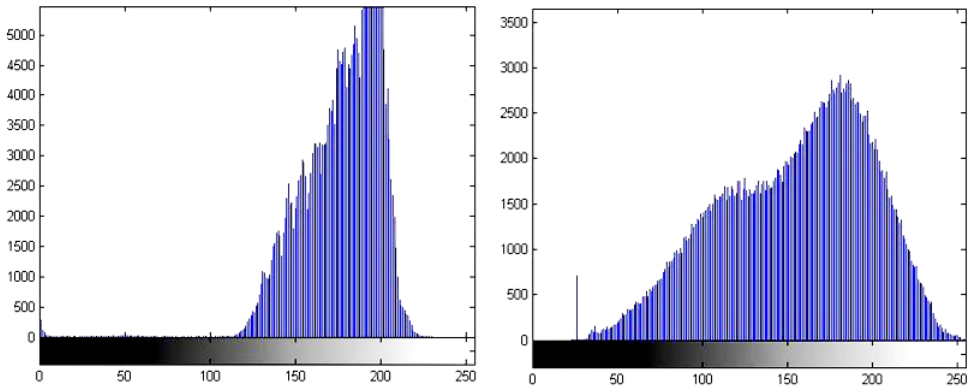

Figure 5.5: From left to right, histogram of Figure 5.3 and histogram of Figure 5.4

5.2.2 Vessel Enhancement

The preceding preprocessing steps improve the distinction of blood vessels and tissues from the background, yet using the previous step, the capillaries and small blood vessels cannot be separated from large blood vessels and other objects such as air bubbles. In this stage, further operations to filter microvascular structures using vesselness criteria are performed on the video frames.

In this approach, vessels are defined as 2-dimensional tubular structures of various sizes. Despite being of different sizes, capillaries can be identified through the same linear structure. Therefore, the measurement scale to define a capillary needs to be based on the structure while disregarding the size. Frangi et al. has developed a vessel enhancement technique founded on this concept [33]. The method characterizes vessel structure in a formula for

vessel enhancement regardless of vessel size. An improved variation of Frangi measure is used in this research.

It is prevalent to use Taylor expansion in order to analyze the geometrical shape of objects such as a vessel in an image. Equation 5.5 is a representation of an image $I(x)$ in the neighborhood of pixel x_o:

$$I(x_o + \delta x_o, \sigma) \approx I(x_o, \sigma) + \delta x_o^T \nabla_{o,\sigma} + \delta x_o^T H_{o,\sigma}\, \delta x_o \tag{5.5}$$

In Equation 5.5, $\nabla_{o,\sigma}$ and $H_{o,\sigma}$ are the gradient vector and Hessian matrix of the image at point x_0 and scale σ respectively. The Taylor expansion is an approximation of the structure of the image up to second order. The differential operators of $I(x)$ is calculated using the concept of linear scale-space theory in the form of the convolution presented in Equation 5.6:

$$\frac{\sigma}{\sigma x} I(x, \sigma) = \sigma^{\gamma} I(x) * \frac{\partial}{\partial x} G(x, \sigma) \tag{5.6}$$

where the D-dimensional Gaussian function is in the form of:

$$G(x, \sigma) = \frac{1}{(2\pi\sigma^2)^{\frac{D}{2}}} e^{\frac{-\|x\|^2}{2\sigma^2}} \tag{5.7}$$

In Equation 5.6, γ describes a family of normalized derivatives which is essential for effective comparison of the response of differential operators at different scales. The second order derivatives of a Gaussian kernel at a particular scale creates a probe kernel that measures the contrast in the given range and outside that, $(-\sigma, \sigma)$, in the direction of the derivative.

$$\delta x_o^T H_{o,\sigma}\, \delta x_o = (\frac{\partial}{\partial \delta x_o})(\frac{\partial}{\partial \delta x_o}) I(x_o, \sigma) \tag{5.8}$$

Equation 5.8 describes the second order directional derivative. Local second order structure of the image is decomposed using eigenvalue analysis of the Hessian. Assume that $\lambda_{\sigma,k}$ is the eigenvalue corresponding to the kth normalized eigenvector $\widehat{U}_{\sigma,k}$ of the Hessian at scale σ.

Since eigenvalue is defined by:

$$H_{o,\sigma}\,\widehat{U}_{\sigma,k} = \lambda_{\sigma,k}\,\widehat{U}_{\sigma,k} \tag{5.9}$$

From Equation 5.9, it can be derived that:

$$\widehat{U}^{T}_{\sigma,k} H_{o,\sigma}\,\widehat{U}_{\sigma,k} = \lambda_{\sigma,k} \tag{5.10}$$

Using Equation 5.9 and Equation 5.10, two orthogonal eigenvalues of λ_1 and λ_2, ($|\lambda_1| \leq |\lambda_2|$) can be extracted. The eigenvalues are invariant up to a scaling factor when mapped by the Hessian matrix. A spherical neighborhood with the center of x_o and radius of $(1, N_{xo})$ will be mapped to an ellipsoid with axes corresponding to the same direction and magnitude of the eigenvalues. The ellipsoid describes the second order structure of the image. The relation between the eigenvalues is used to detect different structures in an image. In order to detect vessels, one has to verify that λ_1 is a small value and λ_2 is a large value. The eigenvectors of $\widehat{U}_1$ and $\widehat{U}_2$ corresponding to λ_1 and λ_2, indicate the minimum intensity variation (the direction of vessel) and maximum intensity variation (the direction of edge) respectively.

In SDF video frames, the vessels can be observed as 2-dimensional tubular dark objects in a less darker background. To determine the likelihood of an object being a vessel, the following relation should hold:

$$\|\lambda_1\| \approx 0 \tag{5.11}$$

$$\|\lambda_1\| << \|\lambda_2\| \tag{5.12}$$

Additionally, a ratio is defined as follows:

$$R_B = \frac{\|\lambda_1\|}{\|\lambda_2\|} \tag{5.13}$$

The ratio in Equation 5.13 becomes maximum for a blob-like object and zero $\lambda_1 \approx 0$. Another ratio S, the norm of Hessian, is defined as follows:

$$S = \|H\| = \sqrt{\lambda_1^2 + \lambda_2^2} \tag{5.14}$$

The eigenvalues for a background pixel are smaller than a vessel pixel, since the changes in the contrast, for background pixels is less than that of vessel edge pixels. This concept is quantified through Equation 5.14.

Using the above mentioned properties and definitions, a vessel likeliness function, called Frangi is characterized as follows [33]:

(5.15)

$$V_o(s) = \begin{cases} 0 & if\ \lambda_2 > 0 \\ e^{-\frac{R_B^2}{2\beta^2}}(1 - e^{-\frac{S^2}{2c^2}}) & otherwise \end{cases}$$

In Equation 5.15, β and c are threshold values that control the sensitivity of the filter to R_B and S. The parameters are combined in a way that the output of the function is maximum for a vessel structure. Confirming what was also suggested by the original Frangi, experiment has shown that β value equal to 0.5 along with c value equal to 0.5 create the best results. The Hessian matrix is formed for σ values from 1 to 10. Figure 5.6 illustrate the result of applying the vessel enhancement technique to a microcirculation sample frame.

The original Frangi technique is effective in detecting vessel-like structures, however it results in emergence of artifacts in the background as can be observed in 5.6. Accordingly, the parameters and components of the function are modified in order to obtain more effective results. Research and experiments on the functionality of the parameters and components

has shown that the λ values directly affect the output of the function. Hence, to improve the current results, the value of λ increases exponentially. The vesselness function introduced in the new method alters the Frangi function by highlighting the roles of λ by changing its exponential role to a 'double exponential' role as shown in Equation 5.17. Variations of the function with different rates of increase in λ values were created to test their effects on the results. The experiments show that double exponential increase of the λ values significantly improves the results, while decreases the presence of artifacts caused by the original Frangi filter. Furthermore, the components of S and $1 - e^{-\frac{S^2}{2c^2}}$ are changed as follows:

$$S' = \|H\| = (\lambda_1^2 + \lambda_2^2)^2 \tag{5.16}$$

$$V_o'(s) = \begin{cases} 0 & if\ \lambda_2 > 0 \\ exp^{-\frac{R_B^2}{2\beta^2}}(1 - e^{-\frac{S'^2}{2c^2}})^2 & otherwise \end{cases} \tag{5.17}$$

Figure 5.7 presents the results of applying the function in Equation 5.17 to Figure 5.4. It is evident that the amount of artificial noise added to the image due to vessel enhancement is considerably lower in the proposed modified Frangi filter than the original Frangi filter.

5.2.3 Edge Enhancement

The prior steps lead to considerable improvement in identification of blood vessels in video frames. However, while the output of the operations presents both large and small blood vessels, the blood vessel edges and curvatures are blurry. Since the study focuses on correct detection of small blood vessels, it is crucial to eliminate large blood vessels and reinforce the intensity value of blood vessel edges. For that purpose, the method presented in [37] is

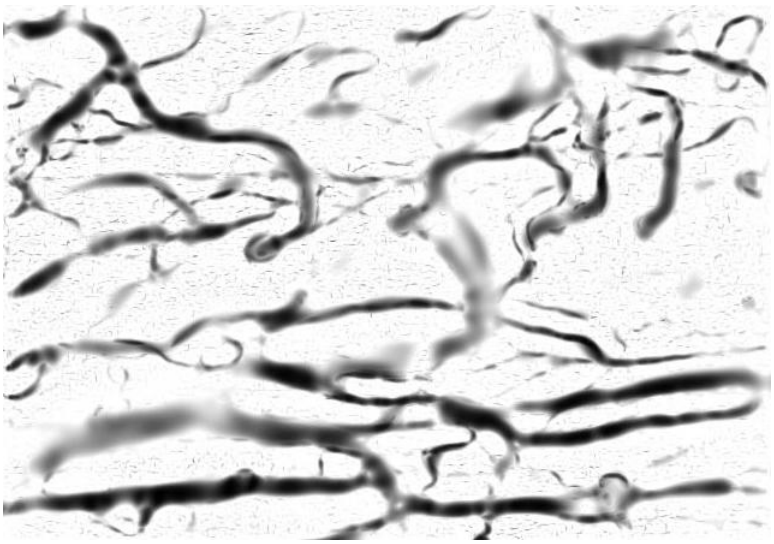

Figure 5.6: Result of enhancing the vessels in Figure 5.4 using original Frangi filter

applied to the results of the vessel enhancement step. The method has been founded on three properties of blood vessels:

(a) Blood vessels are line-like objects connected to each other with small or big curvatures to form blood vessel networks. In order to preserve the curvatures, anti-parallel pairs of lines are approximated by piecewise linear segments.

(b) As can be seen in the results from the vessel enhancement section, blood vessels appear darker than the background. Studies of the intensity profile of blood vessels have shown that the profile can be approximated by the following Gaussian curve:

$$f(x,y) = A\left\{1 - ke^{\frac{-d^2}{2\delta^2}}\right\} \tag{5.18}$$

In Equation 5.18, d is the perpendicular distance between point (x, y) and the straight centerline of the blood vessel, δ is the distribution parameter in the intensity profile, A is the graylevel of the local background and k is the ratio of the intensity of the blood vessel to that of the local background.

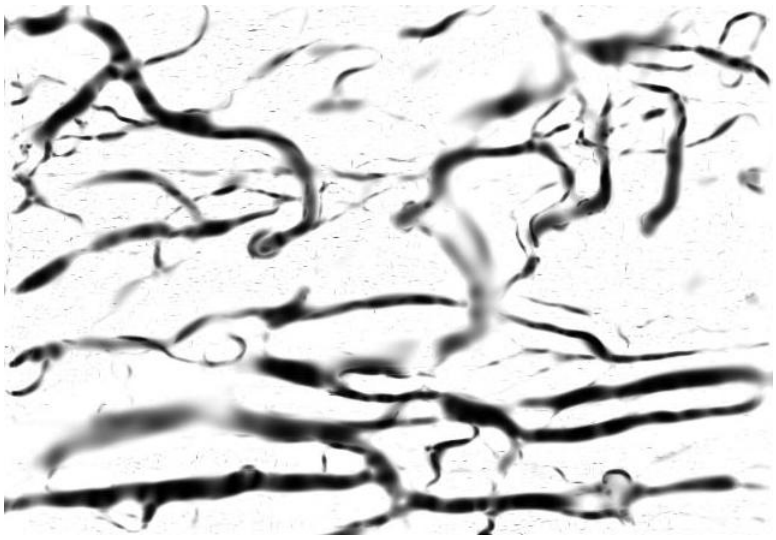

Figure 5.7: Result of enhancing the vessels in Figure 5.4 using the proposed variation of Frangi filter

(c) The width of microvessels varies from one to another. Studies of vessel sizes indicated that the width falls within the range of 2-10 pixels which is equivalent of 20 to 100 μm.

In a microcirculation frame, blood vessels may be seen in any orientation with any θ angle ($0 \leq \theta \leq \pi$) with respect to X and Y axis. A filter to cover all vessels with any orientation needs to be rotated to correspond to $\theta \pm \frac{\pi}{2}$ angles. Therefore, the 2-dimensional matched filter kernel in Equation 5.19 is convolved with each image and the maximum response is kept as the filter response. To improve the time-complexity of the process, a number of cross sections are matched concurrently instead of matching single intensity profile of the cross section of a vessel. In this case, ten 15×16 pixel kernels are convolved with the image. As a result of this operation, edges of small blood vessels are enhanced, meanwhile large blood vessels and tissues become part of the background.

$$f(x,y) = e^{\frac{-x^2}{2\sigma^2}} for |y| \leq \frac{L}{2} \tag{5.19}$$

In 5.19, L is the length of the selected segment of the vessel with fixed orientation. The value of L is determined by experiment through the analysis of large and small blood vessels. For the experiment, a number of blood vessels are visually examined to find the number of pixels (length) that present a sufficient portion of a small blood vessel and $L = 20$ satisfies this requirement. Since the intensity of pixels belonging to background in vessel enhancement output is mostly uniform with zero mean Gaussian white noise, the expected filter response is ideally zero for background pixels. Figure 5.8 shows the edge enhancement result for a microcirculation frame.

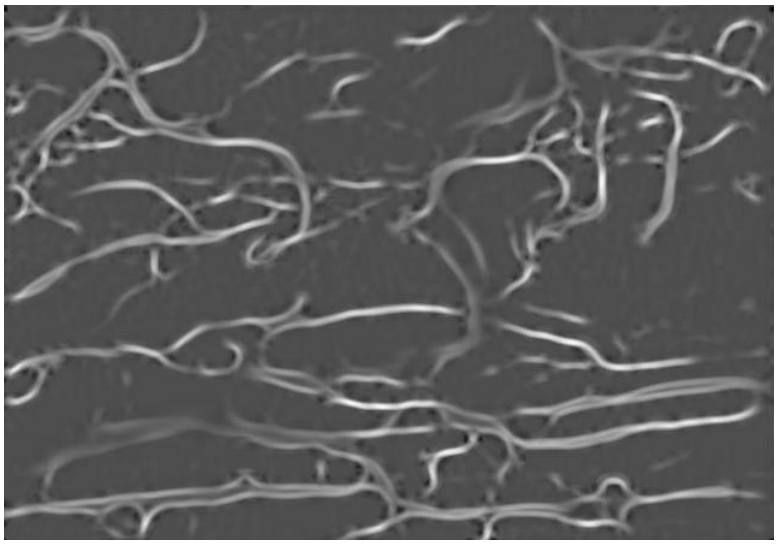

Figure 5.8: Result of edge enhancement of Figure 5.7

Chapter 6

Segmentation

6.1 Overview

This chapter describes the image segmentation methodology. The main step of segmentation is finding a threshold value that partitions the image into small blood vessels and background. The thresholding technique used is based on entropy. This chapter provides a detailed description of the thresholding and its results. Figure 6.1 provides a summary of the method.

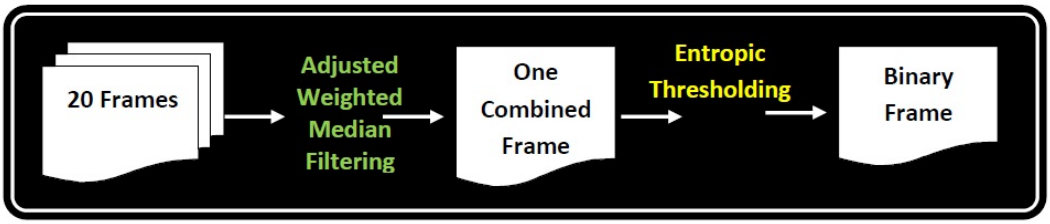

Figure 6.1: Diagram of the proposed segmentation technique

6.2 Description of the Method

The aim of segmentation is to distinguish between background and foreground in a video frame, and to identify active blood vessels and capillaries among other foreground objects. In

segmentation, the results of video enhancement are combined through a variation of median filtering. Following that, a novel entropic thresholding technique is applied to a set of 20 consecutive frames to calculate the optimal threshold. Then, the combined frame is thresholded to generate the resulting binary frame.

6.2.1 Adjusted Weighted Median Filter

Prior to thresholding, a set of 20 enhanced frames are combined through an Adjusted Weighted Median Filter (AWMF). The well-known median filter is a special form of WMF with no weight added. Median filtering is usually used for preprocessing of image processing applications to remove noise; however, the proposed method uses AWMF for pixel-by-pixel combination across 20 frames. The AWMF in this method removes the noise from the frames in which some pixels are mistakenly assigned to vessels or background.

To consider only the immediate neighbors of a point, a filter of size 3 ($n = 3$) was selected for this study. For a filter of $n \times n$ pixels, the median filter begins with sorting the numbers. The centroid number is the $\left\lceil \frac{n \times n}{2} \right\rceil + 1$ th element in the sorted array. In conventional median filtering, the numbers in the defined window are sorted and the centroid is replaced with the median of the numbers. Weighted median filtering creates more flexibility to control the properties of the filter compared to the regular median filter. Regular WMF has a component called "Weight Index" (WI) that defines the number of times that the centroid element is copied to the sorted array. The parameter WI is not used in this experiment. In the proposed AWMF, a "Shift Index" (SI) is defined to adjust the WMF according to the particular application. SI allows for setting a bias in the filter. The bias can be used as a factor to dominate black pixels over white ones or vice versa. SI is a real number in the range

of [0 1] that defines the percentage of shifting to the right or left from the centroid in the sorted array. In other words, the new median is not the median in the sorted array but it is the $\lceil n \times n \times SI \rceil$th element. Considering a binary image, any SI lower than 0.5 prefers zeros to ones and any SI greater than 0.5 prefers ones to zeros, considering equal number of zeros and ones. An example of the effect of SI on a 3×3 window in a binary image is as follows:

Original array: 0 1 0 1 0 0 0 1 1

Sorted array: 0 0 0 0 0 1 1 1 1

Without SI	Median=0
SI = 0.9	Median=1
SI = 0.2	Median=0

This algorithm is applied to each pixel at coordinate (x, y) across 20 frames. For each coordinate, 20 values are available. The values are sorted and the resulting adjusted median pixel is selected as the final result of combining the 20 frames. Analysis of the statistical measures of mean, median and standard deviation of different values of SI has shown that SI values of 0.1, 0.3, 0.6 and 0.9 generate the best results. The value of SI changes adaptively, looking at the mentioned statistical measures. The adjusted weighted median filtering combines the frames and improves the connectivity/ continuity of the blood vessels accordingly. Figure 6.2 presents the result of applying AWMF to a set of 20 microcirculation frames.

6.2.2 Thresholding

Bi-level thresholding is the simplest image processing technique for converting a grayscale or a color image to a binary image. The conversion is performed using a threshold value. If the intensity value of a pixel is less than or equal to the threshold value, the corresponding pixel in the output image is set to black (white), otherwise it is set to white (black). The challenge

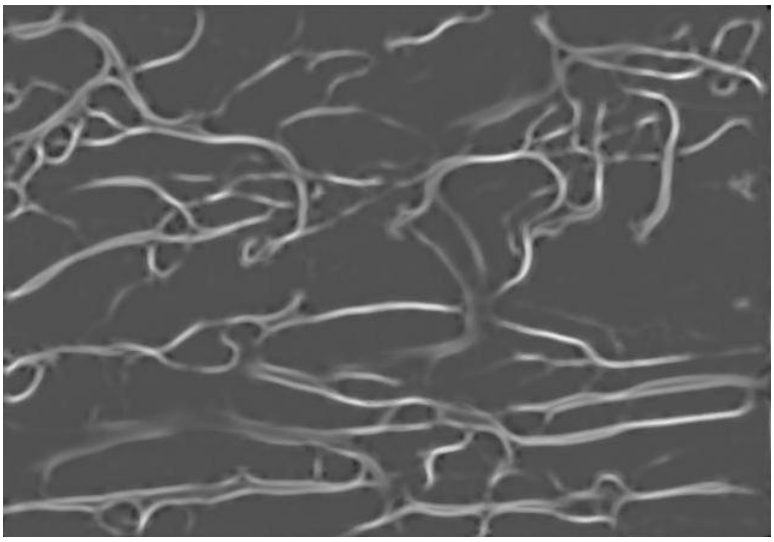

Figure 6.2: Result of combining 20 consecutive video frames using AWMF

in thresholding is to choose an optimal threshold value that results in the least information loss.

In microcirculation images, the blood vessels are of different intensity values and this complicates the thresholding process. Global thresholding creates poor results if used for such images, thus local thresholding is utilized. The local thresholding technique used in this study is based on Gray Level Spatial Correlation Histogram. The technique effectively preserves spatial structure of the image considering neighborhood similarity of each pixel

Consider $f(x, y)$ to be the gray level intensity of a pixel at (x, y) coordinate in the image F of size Q pixels. The element $g(x, y)$ is the number of pixels in N neighborhood of pixel (x, y) within its ϵ distance. The neighborhood information provides a measure for the degree of similarity of a point to its immediate neighboring points. The smaller the value of N, the smaller the neighborhood. The choice of N depends on the contents of the image and is set to 3 in this study. In the video processing section, a flow parameter was calculated for each video frame. The sum of the flow factors for the 10 preceding video frames of each frame,

$Sd(f_i)$, is calculated as shown in Equation 6.1:

$$Sd(f_i) = \sum_{n=i-10}^{n=i} d(f_n, f_{n+1}),\ 10 < i < 21 \tag{6.1}$$

The term $d(f_n, f_{n+1})$ indicates the distance between nth frame (f_n) and $n+1$th frame (f_{n+1}), calculated after the stabilization. Since the value of the sum changes over a rather wide range, it needs to be adjusted in order to be effectively used. Two categories are defined for the adjustment. One category entails the sum values that are within one standard deviation above and one standard deviation below the given sum value. The other category contains the remaining sum values.

The Gray Level Spatial Correlation Histogram of the image is the probability value for each combination of the three mentioned factors. It is calculated as follows:

$$h(k, m, D) = prob(f(x, y) = k, g(x, y) = m, Sd(f) = D) \tag{6.2}$$

$$f(x, y) \in \{integers:\ 0 - 256\}$$

$$g(x, y) \in \{integers:\ 1 - 9\}$$

$$Sd(f) \in \{1\ or\ 2\}$$

where $f(x, y)$ is the intensity of the image at (x, y), $g(x, y)$ is the number of neighboring pixels within ϵ difference from a pixel (including the pixel itself) and $sd(f)$ is the sum of the flow factor for each frame. The probability $h(k, m, D)$ is calculated for each frame $256 \times 9 \times 2$ times, bringing into account any possible combination of $f(x, y)$, $g(x, y)$ and $Sd(f)$.

According to the principle of entropy, noise and edges produce a higher entropy value than objects and background. The image will still contain some noise that was not removed in the previous steps. For that reason, a weight factor is computed using the following nonlinear

function:

$$W(m,N) = \frac{(1+e^{\frac{-9m}{N\times N}})}{(1-e^{\frac{-9m}{N\times N}})} \tag{6.3}$$

This weight function emphasizes the effect of neighborhood information by adding N to the equation and adjusting it using m, the possible values for $g(x,y)$.

The technique to calculate the threshold tries to find the threshold value $T > 0$, that maximizes the entropy of objects and background. T divides the image into object (O) and background (B). The second order entropies defined through the following equations lead to the discovery of T:

$$H_B(T,N) = -\sum_{k=T+1}^{256}\sum_{m=1}^{N\times N}\frac{P(k,m,D)}{P_B(T)}ln\frac{P(k,m,D)}{P_B(T)}W(m,N) \tag{6.4}$$

$$H_O(T,N) = -\sum_{k=0}^{T}\sum_{m=1}^{N\times N}\frac{P(k,m,D)}{P_O(T)}ln\frac{P(k,m,D)}{P_O(T)}W(m,N) \tag{6.5}$$

$H_B(T,N)$ is the notation for the second order entropy of the background and $H_O(T,N)$ for that of the object. From Equations 6.4 and 6.5, the total second order entropy is calculated as follows:

$$H(T,N) = H_O(T,N) + H_B(T,N) \tag{6.6}$$

The entropy is calculated for the set of 10 frames and the maximum entropy for each frame is kept. Although the objective is to acquire the T value that maximizes $H(T,N)$, the effect of background noise and noise factors such as outliers causes a reduction in the accuracy of the calculated threshold value. To offset this effect, the median of ten values is selected as the final T.

Following the selection of the optimized threshold value based on 10 frames, the resulting combined frame from the previous step is thresholded. Thresholding partitions the image

into two parts: foreground and background. The foreground consists of capillaries and small blood vessels and the background is the remaining part in the image. For thresholding, all pixels belonging to foreground are set to zero and the rest of the pixels are set to one.

Figure 6.3 illustrates the thresholding result for the AWMF frame. The resulting binary video frame need to be post-processed in order to generate the final results.

Figure 6.3: Result of thresholding of Figure 5.8

Chapter 7

Post-processing

7.1 Overview

This chapter describes the post-processing technique. A region growing technique based on image gradient information to deal with the discontinuity of blood vessels is implemented for post-processing. As the final step, Functional Capillary Density is calculated for the resulting image.

7.2 Description of the Method

Prior to being thresholded, the video frames are combined with AWMF. Although effective, the thresholding result might miss part of vessels when thresholding the combined frame. The goal of post-processing is to refine the thresholding results through assigning new pixels either to background or to vessels based on some predefined criteria. The regions grow using an iterative relaxation technique. Following region growing, the quantitative measure of Function Capillary Density (FCD) is calculated, which is defined as the area of vessels divided by the area of the background. Figure 7.1 demonstrates the proposed techniques in this section.

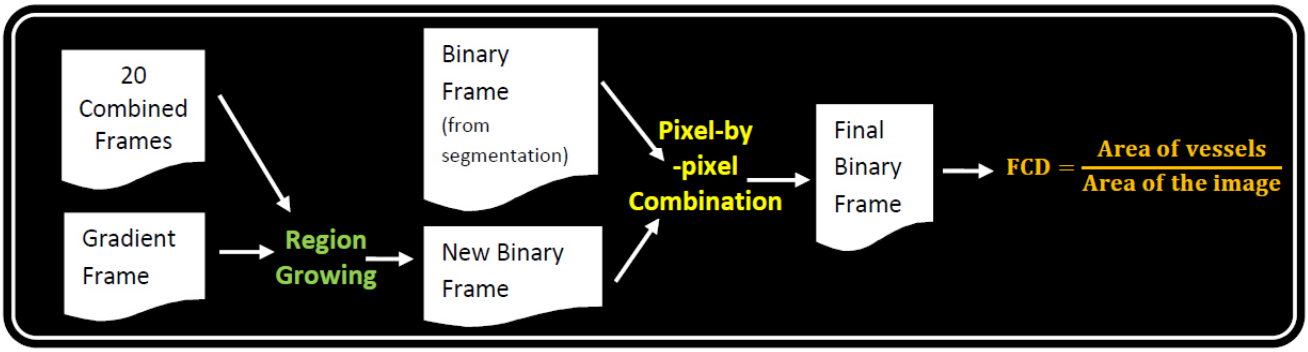

Figure 7.1: Diagram of the proposed post-processing technique

7.2.1 Region Growing

The region growing technique used is a modification of the method proposed in [52]. The algorithm uses the gradient magnitude (γ) and the grayscale intensity value (k) of the combined frame to define the criteria for classifying pixels as vessel or background. The region growing occurs in two stages. In the first stage, the classes grow in regions with low gradient magnitude, allowing for a rather quick classification. In the second stage, the classification constraint is relaxed, allowing the classes to grow based on the intensity value of the combined frame. The first stage suppresses growth in edge regions , where the magnitude of gradient is high, and the second stage defines borders between regions.

Low gradient is defined as $\gamma < \mu_g + \sigma_g$, where μ_g is the mean of the gradient magnitude and σ_g is the standard deviation of that. k is automatically divided into two classes of vessel and background based on its graylevel histogram. It is simply thresholded using the Otsu thresholding technique [53]. Otsu is a nonparametric method and computes a global threshold by minimization of interclass variance of black and white pixels in the resulting binary image. The thresholding technique uses the zeroth and first -order moments of the graylevel histogram. Following thresholding, the mean and standard deviation for the vessel

class, μ_v and σ_v, along with the mean and standard deviation for the background class, μ_b and σ_b are calculated. One more parameter to set is the size of the interval (α) for each class in each iteration.

The algorithm starts with selecting the seed points for the regions. Background seeds and vessel seeds are defined as the pixels with the following properties:

Background seeds: $k \leq \mu_b$

Vessel seeds: $k > \mu_b$

In the initial image, background, vessels and unlabeled pixels are shown in gray, black and white pixels respectively. Figure 7.2 illustrates an instance of initializing seeds in a microcirculation frame.

Figure 7.2: Initial selection of seeds in a microcirculation frame

After creating the initial image, the iterative region growing process starts with assigning label to unlabeled pixels. In the first stage, unlabeled pixels are classified as vessel through the following condition:

$$(\mu_v - \alpha_v \sigma_v) \leq k \; AND \; \gamma \leq (\mu_g + \alpha_g \sigma_g) \; AND \; N_v \geq 1 \tag{7.1}$$

where N_v is the number of neighboring pixels already labeled as vessel and α_v is the interval whose initial value is 0.5 and is incriminated by 0.5 in each iteration. Alternatively, the unlabeled pixels are classified as background through the following condition:

$$k \leq (\mu_b - \alpha_b \sigma_b) \; AND \; \gamma \leq \mu_g \; AND \; N_v \geq 1 \tag{7.2}$$

where N_b is the number of immediate neighboring pixels already labeled as background and α_b is the interval whose initial value is 0.5 and is incriminated by 0.5 in each iteration. The two steps are alternated until no unlabeled pixels are found to classify using properties in Equation 7.1 and Equation 7.2.

In the second stage, vessel and background are classified concurrently regardless of their gradient magnitude. The condition for classifying a pixel as vessel is:

$$(\mu_v - \alpha\sigma_v) \leq k \leq (\mu_v + \alpha\sigma_v) \; AND \; N_v \geq 1 \tag{7.3}$$

and for background is:

$$(\mu_b - \alpha\sigma_b) \leq k \leq (\mu_b + \alpha\sigma_b) \; AND \; N_b \geq 1 \tag{7.4}$$

where α is the interval with the initial value of 0.5 which increases by 0.5 in each iteration. This step is iterated until there is no further pixel to be classified as vessel or background.

The resulting image from region growing step is combined with the result of thresholding from the segmentation section. If a pixel is categorized as vessel in one of the images, the pixel is labeled as vessel, otherwise it is labeled as background. Figure 7.3 presents the result of post-processing for a healthy subject.

7.2.2 Functional Capillary Density

As the final step, Functional Capillary Density (FCD) is calculated for the binary result of post-processing. FCD is a quantitative factor that can be used as a determinant of condition of microcirculation in the body [16]. FCD is computed as the total area of capillaries divided by the area of the whole image. In the resulting binary images, FCD is calculated as follows:

$$FCD = \frac{Area\ of\ vessels}{Area\ of\ the\ image} \tag{7.5}$$

The calculated FCD values for 97 videos are provided in the result section.

Figure 7.3: Result of post-processing of Figure 6.3

Chapter 8

Results

The described algorithm was applied to 124 microcirculation video samples taken with MicroScan and provided by Virginia Commonwealth University, Department of Emergency Medicine. The sample videos were captured from human and animal subjects. Virginia Commonwealth University Reanimation Engineering Science Center (VCURES) performed sample preparation and FCD scoring for most of the sample videos. The device used for capturing the samples guarantees a fixed distance of $1mm$ from sublingual tissue surface. The Microscan system has a Gaussian point spread distribution with standard deviation of 1 pixel in x and y directions. The rate of capturing videos is 29 frames per second.

To verify the capabilities of the algorithm in segmenting capillaries and small blood vessels, it was applied to two sets of sample data. The first dataset belongs to 97 human subjects. The subjects were patients under supervision in the Intensive Care Unit (ICU) with a heart failure condition. The microcirculation videos for this group were recorded at different times during their hospital stay. The videos were analyzed by eight physicians, using the commercially available software AVA. As mentioned in chapter 2, this software is not capable of automatic analysis of microcirculation videos and requires human interaction. AVA starts with default

parameters for the analysis of microcirculation videos. The parameters can be adjusted as the user observes the results of the analysis on computer screen. The initial segmentation and analysis performed by AVA is almost always inaccurate and is referred to as "Unedited AVA Produced FCD", the user is expected to spend a significant amount of time, often between 20 to 30 minutes, editing the segmentation parameters and deriving accurate FCD results. The final results used by researchers and clinicians are therefore AVA produced results which are heavily-edited and corrected by the human expert and are referred to as "Heavily-Edited AVA Produced FCD". Heavily-Edited AVA Produced FCD is considered the gold standard for this study and the algorithm results were evaluated based on that.

None of the physicians analyzed all 97 videos; hence, for each video either 2 or 5 FCD values are available. A comparison between the results provided by experts and those of the algorithm was performed to verify the reliability of the proposed method. The segmentation results of applying the algorithm to 3 human subjects are presented in Figure 8.1. The FCD values calculated by the algorithm for the subfigures in the first, second and third row are 14.2%, 16.64% and 15.11% respectively, whereas the results of the manual analysis of the same subfigures by AVA are 15.6%, 19.4% and 15.7%. As can also be seen visually, the segmentation results show the majority of capillaries and small blood vessels in the original frames. Furthere more, tissue and background noise were effectively removed during the image processing steps.

For further assessment of the calculated results by the algorithm, Bland-Altman plot (Difference plot) is used. This method is commonly used in medical statistics to compare the difference between the results acquired by two comparable techniques/ treatments [54]. In a Bland-Altman plot, the x-axis shows the mean value of the techniques, the y-axis shows the

difference between the values of the techniques, and the mid-line shows the mean value of the difference. The two horizontal lines, parallel to the x-axis determine a 95% Confidence Interval (CI), calculated by the mean of difference between the two techniques $\pm 1.96\times$ the standard deviation of the difference.

Six bland-Altman plots are provided for this study. The first plot, shown in Figure 8.2, presents the comparison of the algorithm results with those of the median of Heavily-Edited AVA Produced FCD. Median is a reliable statistical measure when multiple values are available for a measurement technique. The second plot, shown in Figure 8.3, demonstrates the comparison of the results of the algorithm with those of the mean of Heavily-Edited AVA Produced FCD. Mean serves as another statistical measure when multiple values are available for a measurement technique. The third plot, shown in Figure 8.4, displays the comparison of the Heavily-Edited AVA Produced FCD by two of the experts. It is important to know how much an instance of Heavily-Edited FCD Produced by AVA might vary from one expert to another. The fourth plot, shown in Figure 8.5, presents the comparison of the algorithm results with the results of the Heavily-Edited AVA Produced FCD by one of the experts (Expert A). The fifth plot, shown in Figure 8.6, displays the comparison of the algorithm results with the results of the Heavily-Edited AVA Produced FCD by another expert (Expert B). The sixth plot, shown in Figure 8.7, presents the comparison of the results of median of Heavily-Edited AVA Produced FCD with the results of Unedited AVA produced FCD. These plots shows how much variability exists between the results of Heavily-Edited Produced AVA, which is produced semi-automatically, and the results of unedited one, which is generated automatically with default parameters. Bland-Altman results will be further analyzed in the discussion chapter.

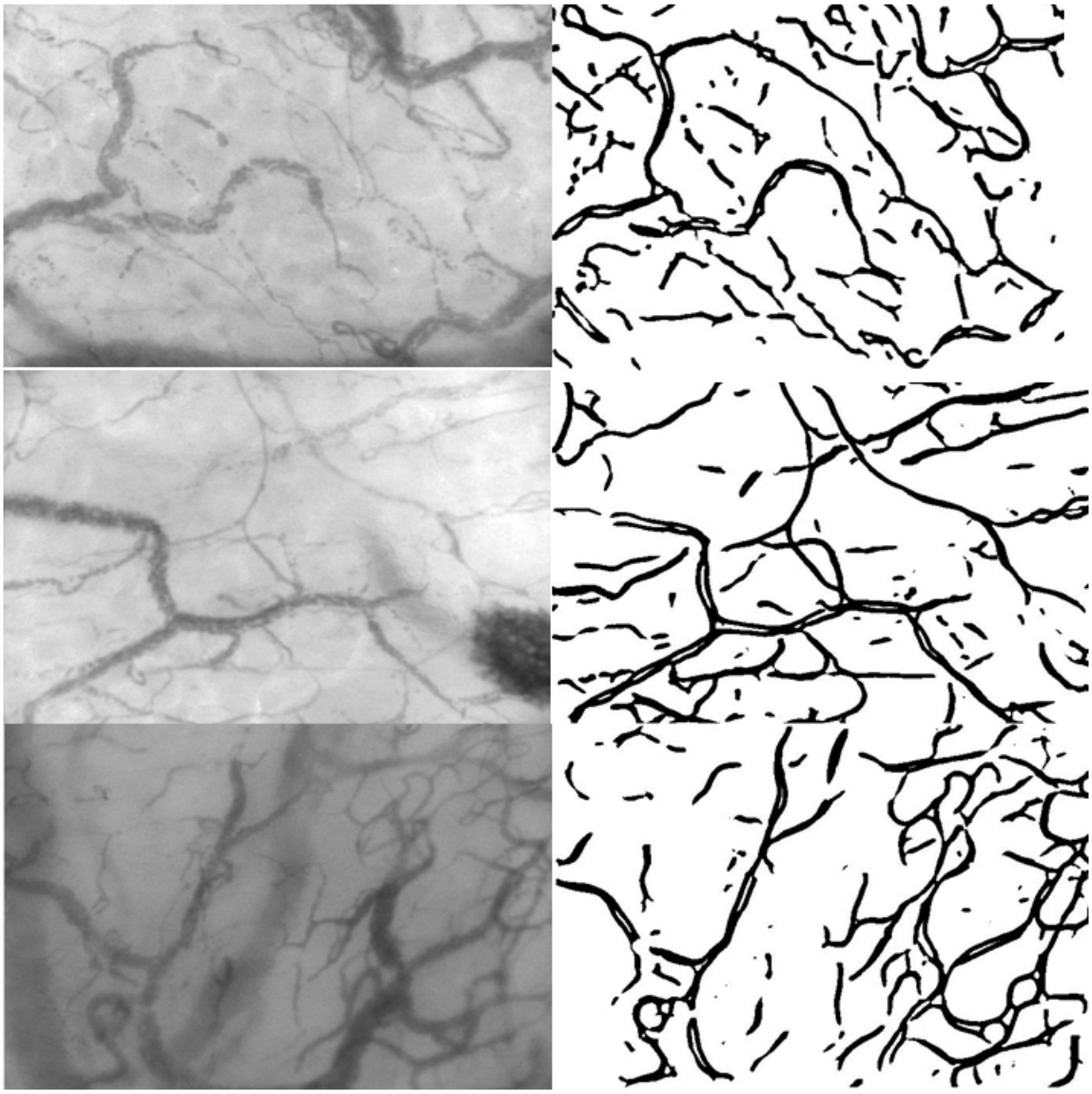

Figure 8.1: Each row shows the original microcirculation frame of a human subject (on the left) and the segmentation result of the frame (on the right)

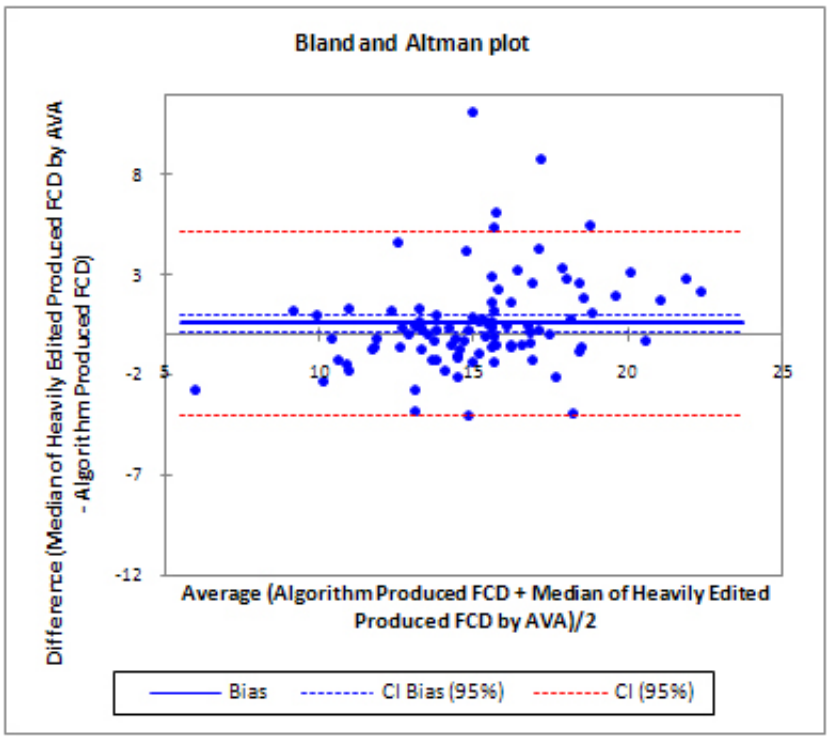

Figure 8.2: Bland-Altman plot, comparison of the algorithm results with that of the median of Heavily-Edited AVA Produced FCD

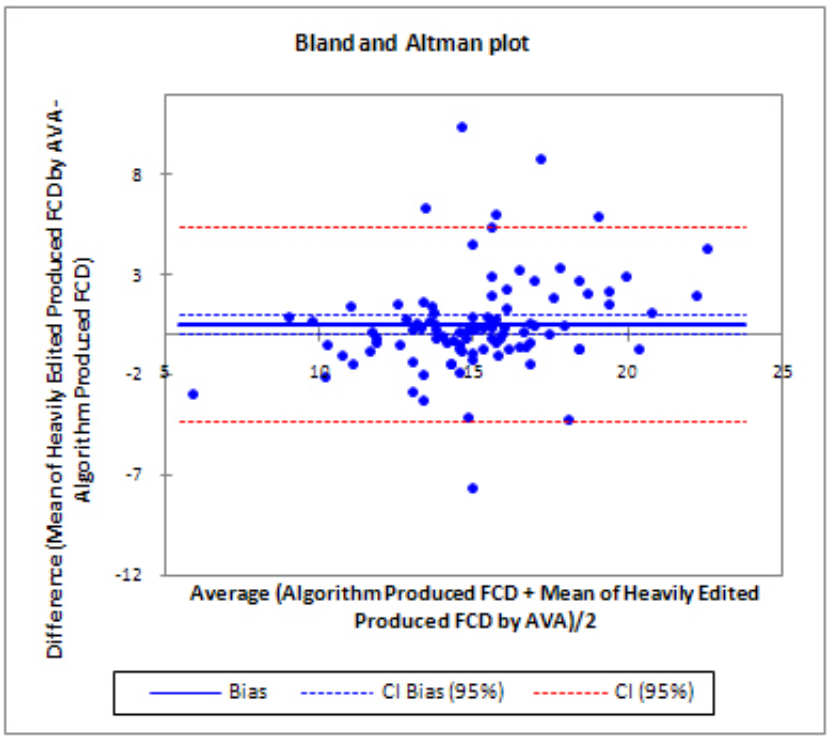

Figure 8.3: Bland-Altman plot, comparison of the results of the algorithm with that of the mean of Heavily-Edited AVA Produced FCD

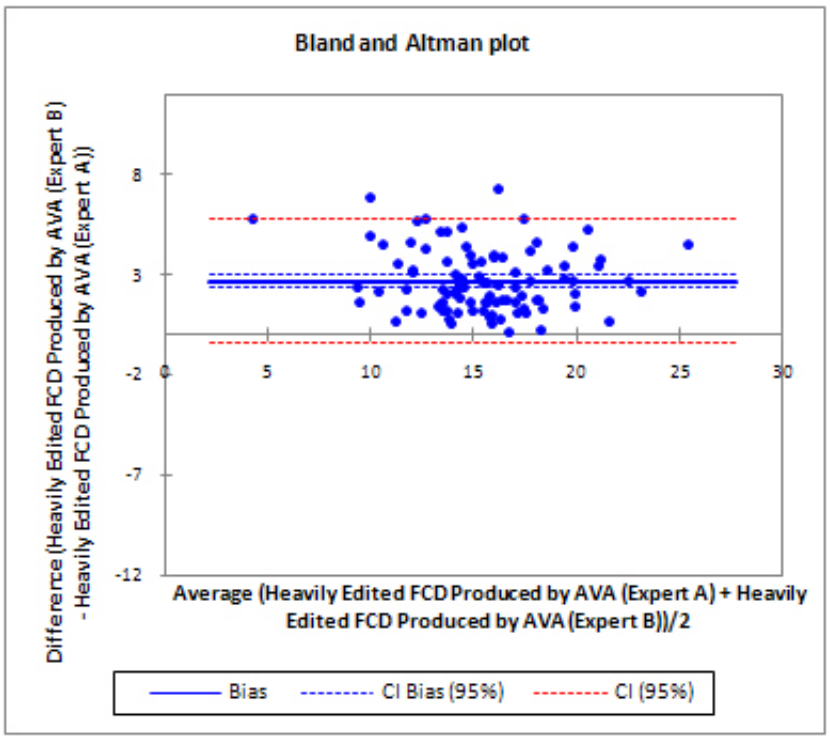

Figure 8.4: Bland-Altman plot, comparison of the Heavily-Edited AVA Produced FCD by two of the experts (Expert A and Expert B)

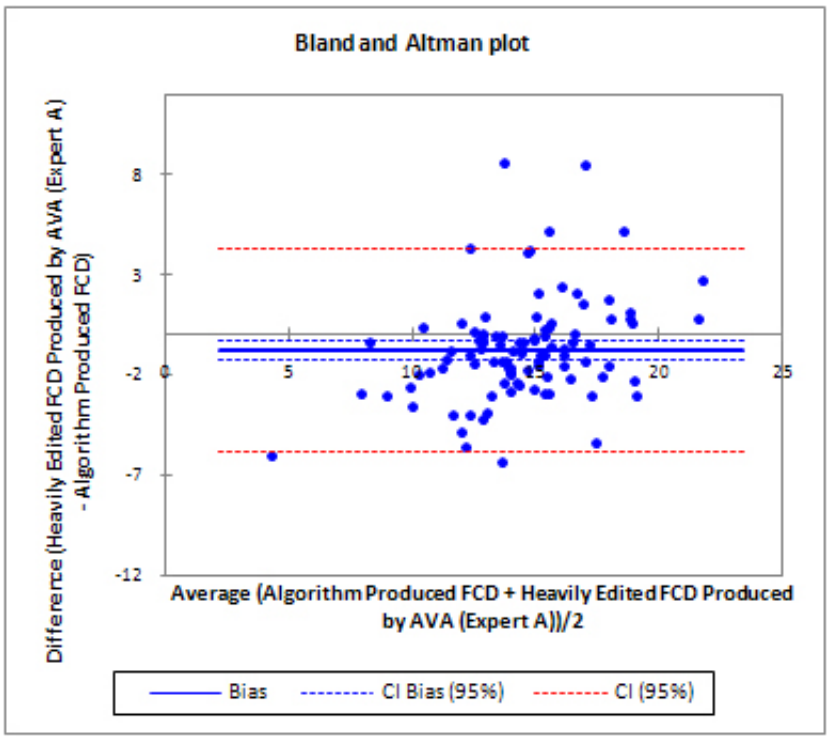

Figure 8.5: Bland-Altman plot, comparison of the algorithm results with that of the Heavily-Edited AVA Produced FCD by one of the experts (Expert A)

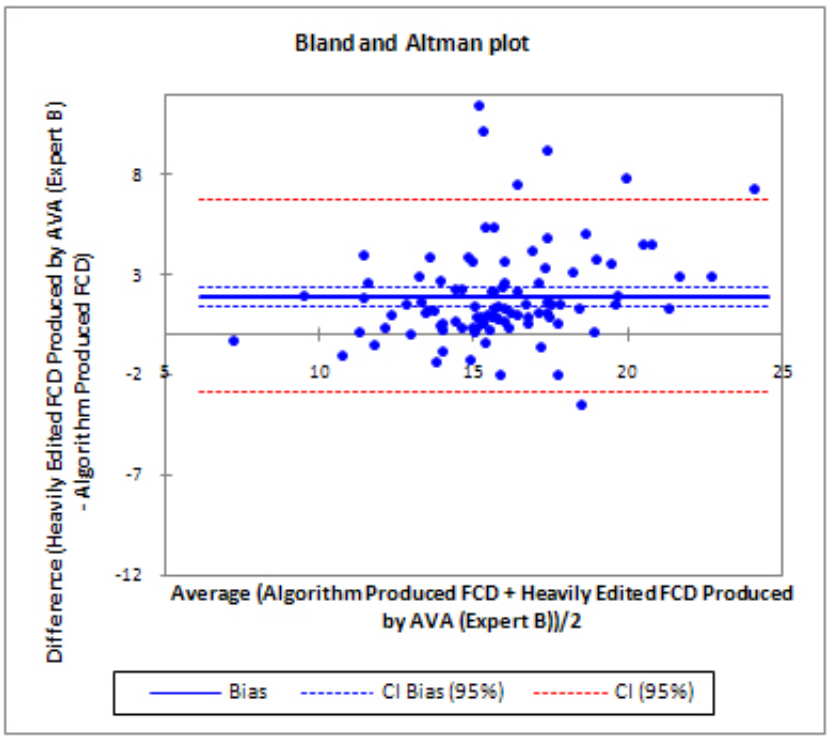

Figure 8.6: Bland-Altman plot, comparison of the algorithm results with that of the Heavily-Edited AVA Produced FCD by another expert (Expert B)

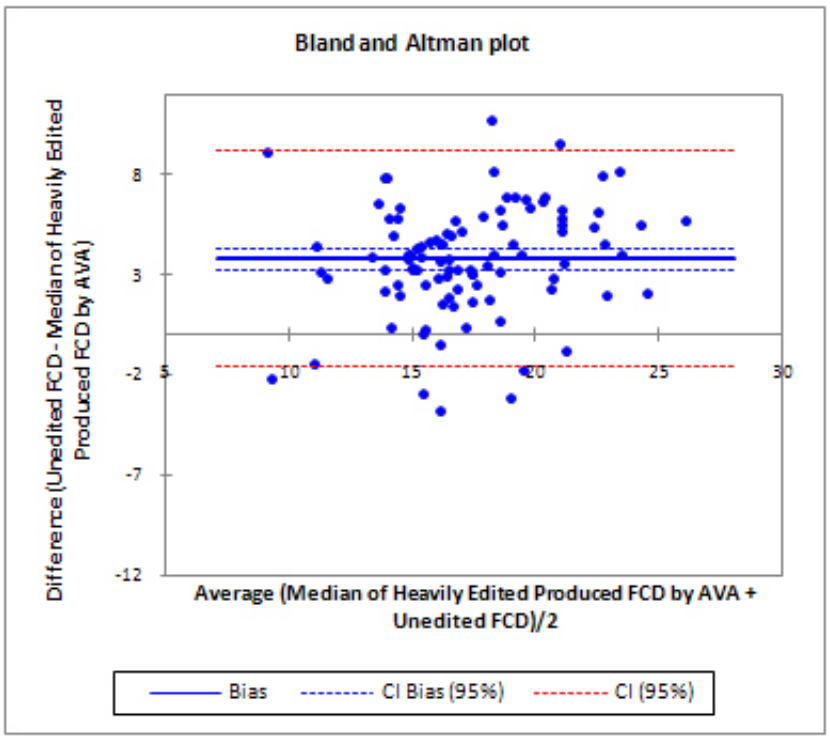

Figure 8.7: Bland-Altman plot, comparison of the median of Heavily-Edited AVA Produced FCD with that of Unedited AVA produced FCD

The table shown in Appendix A exhibits the FCD values for the 97 subjects. The first column presents the FCD values calculated by the algorithm, the second column shows the median of Heavily-Edited Produced FCD by experts, the third column presents the mean of Heavily-Edited Produced FCD by experts, the fourth column shows Heavily-Edited Produced FCD by expert A (one of the experts), and the fifth column presents Heavily-Edited Produced FCD by expert B (another experts). The purpose for using mean and median of Heavily-Edited Produced FCD by experts is to make most use of the provided input by experts (at least 2 and at most 5 FCD values were available for each piece of data).

Table 8.1 presents the mean of difference between Heavily-Edited AVA Produced FCD and the algorithm results, standard deviation of the difference and the upper and the lower 95% confidence interval.

Table 8.1: Mean of difference between Heavily Edited AVA and the algorithm, standard deviation of the difference and 95% interval values

Mean of difference	**STD of the difference**	**Upper 95%**	**Lower 95%**
0.525	2.485	5.396	-4.345

The second dataset contains 12 video samples from healthy and hemorrhaged swine subjects. The number of capillaries is much less in the hemorrhaged subjects than the healthy ones. Fewer capillaries is equivalent to less variation in the histogram of the image, and less variation in the histogram complicates the process of finding an optimal threshold for hemorrhaged subjects since the thresholding method is based on the spatial histogram of the image.

The FCD results for the 12 subjects are presented in table 8.2. The results are based on the processing of 21 frames. The first column contains information about the health status of the subject, the second column is the percentage of FCD values calculated by the algorithm and the third column is the percentage of Heavily-Edited AVA Produced FCD. One comparison

that can be made is based on the difference between the FCD values of the healthy group and the hemorrhaged group.

Table 8.2: FCD Results for 12 Swine Subjects

Subjects	**FCD % by algorithm**	**FCD % by AVA**
Healthy 1	11.71	12.7
Healthy 2	12.09	18.9
Healthy 3	16.72	17.1
Healthy 4	13.65	13.1
Healthy 5	14.15	17.9
Healthy 6	12.47	13.5
Mean	13.47	15.53
Hemorrhaged 1	4.3	8.2
Hemorrhaged 2	4.16	15.1
Hemorrhaged 3	10.71	12.2
Hemorrhaged 4	10.7	11.2
Hemorrhaged 5	8.85	9.5
Hemorrhaged 6	9.23	11.6
Mean	8.00	11.3

Chapter 9

Discussion and Conclusion

9.1 Discussion

MATLAB R2010a was used to implement the proposed algorithm. The algorithm was executed on a Pentium 3, CPU 2.40GHz computer. The computational time to analyze a set of 21 frames with the algorithm was 8 minutes on average. The analysis time can be reduced to less than a minute if the algorithm is implemented in C++, using the OpenCV computer vision library.

Different approaches have been taken by different researchers to study microcirculation extraction and segmentation. The hierarchical algorithm presented in this research is one possible solution to relatively accurate automated analysis of microcirculation videos. This section discusses some of the steps of the algorithm and the algorithm results.

9.1.1 Discussion of Algorithm

(a) Video stabilization is a complex problem with a wide range of solutions. The selection of one method over another depends on the specific application [47]. Among several motion models (transformations) that could be used for video stabilization, rigid body was chosen. In essence, the changes from one microcirculation frame to the following

one in a video is only proper rotation and pure translation, meaning that the sizes and the distances between the objects remain almost the same. Therefore, the proper model for describing the motion in microcirculation videos is rigid body.

(b) The main part of the video enhancement technique, that leads to the identification of vessel-like objects, is the vesselness filter. This filter enhances the vessel-like objects, while reducing the effect of the rest of the objects and the background in a microcirculation frame. The proposed variation of the vesselness filter was founded on a step-by-step experiment. First, the impact of each parameter was studied. Following that, the effect of altering the weight of the parameters in acquiring optimal results was studied. Visual inspection of several frames after changing the weight, in addition to the study of the final results using the modified weight led to the choice of the proposed modifications in the original filter. While lowering the weight of λ, S and $1 - e^{-\frac{S^2}{2c^2}}$ confines the ability of the filter to detect blood vessels correctly, elevating the weight of these parameters erodes small capillaries. The proposed changes provide an appropriate balance between the two alternates.

(c) AVA segmentation results show vessels as continuous line-like objects, even though visual inspection of results shows that some of the vessels are not well-connected. Hence, post-processing is an effective step to improve the results of segmentation by growing the vessels in the areas of discontinuity. Despite being effective, the current region growing technique is insufficient in addressing the issue of discontinuity of blood vessels.

9.1.2 Discussion of Results

(a) The technique is capable of differentiating between healthy and hemorrhaged subjects as can be seen in Table 8.2 as well as Figure 9.3. The cut-off threshold for separating healthy from hemorrhaged subjects is 10%. For further evaluation of this capability of the algorithm, a larger dataset of healthy and hemorrhaged subjects is needed. Figures 9.1 and 9.2 show examples of original image and resulting binary image of a healthy and a hemorrhaged subject respectively.

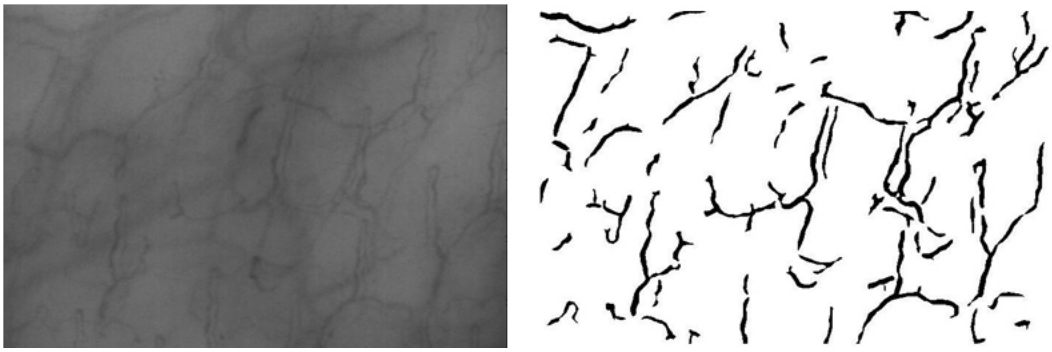

Figure 9.1: From left to right, original image and resulting binary image for a healthy swine subject

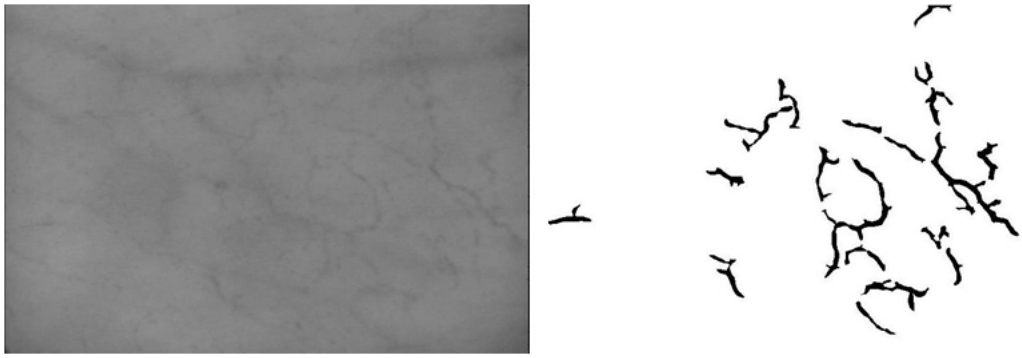

Figure 9.2: From left to right, original image and resulting binary image for a hemorrhaged swine subject

(b) Bland-Altman plot is a common way in the field of medicine to determine whether a new method of measurement is equivalent to an established method that is currently

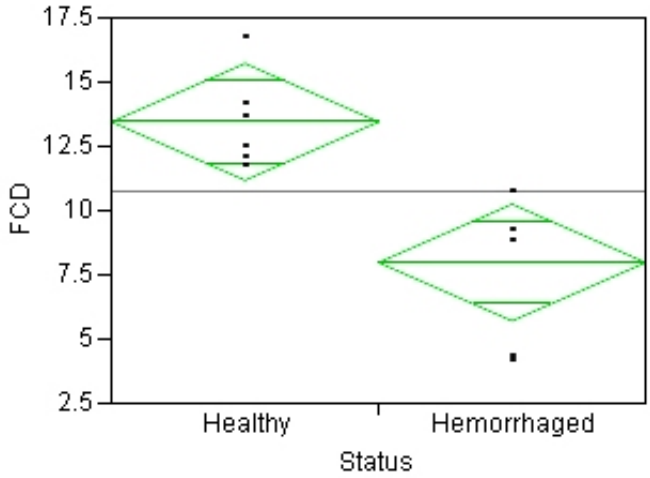

Figure 9.3: One-way analysis of healthy/ hemorrhaged subjects

in use; in other words, if the two methods sufficiently agree, the established method can be replaced by the new method [55]. Bland-Altman plot is used in this study to evaluate the FCD results produced by the algorithm against the gold standard which is another comparable technique (Heavily-Edited AVA Produced FCD). In the plot, x-axis shows the average of the paired values from each measurement and y-axis presents the difference of each pair of measurements.

The blue solid horizontal line presents the bias, which is the mean difference in FCD values obtained with the two measurements. The difference between the blue points above the bias line and the bias is a positive value, while the difference between the blue points below the bias line and bias is a negative value.

The horizontal blue dotted lines show the 95% confidence limits for the bias (limits of agreements by Bland and Altman). The 95% confidence limits of the normal distribution are used to provide the measure of variability of each point from the bias. The confidence limits reprenst the range of values in which agreement between measurements lies for

approximately 95% of dataset.

The red dotted horizontal lines show 95% confidence limits from the mean of the two measurements. The variability of the blue points that are within the 95% confidence limits is acceptable, while the points that are outside the limits are considered outliers. It is unlikely that different methods result in the exact same results for individual measurements [55]. What clinicians wish to know is how much the new method is likely to be different from the old one, so that they can either replace the old method with the new one or use the two methods interchangeably. The comparison of the algorithm results and that of the Heavily-Edited AVA through multiple Bland-Altman plots indicates that the algorithm results are consistent with the results of Heavily-Edited AVA as can be also seen in Figures 8.2, 8.3, 8.5 and 8.6. In the plots, negative bias means that the first method tends to provide a lower value compared to the second one, by the amount between the 95% confidence limits for the bias, while positive bias means that the first method tends to provide a higher value compared to the second one, by the amount between the 95% confidence limits for the bias. For the four mentioned plots, the limits of agreements (95% confidence limits from the mean) are sufficiently small to be confident that the algorithm can be used in place of Heavily-Edited AVA. Overall, they present "Good Agreement" between the two methods [55]. The points outside the red dotted lines are outliers that are 5, 6, 6 and 7 points for the plots in Figures 8.2, 8.3, 8.5 and 8.6 respectively. The outliers are erroronous measurements that are due to the failure of the algorithm in proper segmentation. The denser the points in the plots are, the better the agreement between the two methods is.

The Bland-Altman comparison between the results of Heavily-Edited AVA and Unedited

AVA, Figure 8.7, shows that Unedited AVA Produced FCD, which is calculated automatically, generates results with a wide range of variability. The positive value of the bias indicates that Unedited AVA produces higher FCD values compared to the Heavily-Edited AVA.

(c) The visual quality of frames highly affects the segmentation results. The presence of saliva/ air bubbles, excessive/uneven lighting and lack of proper camera zooming may limit the ability of the algorithm to detect blood vessels accurately. Figure 9.4 shows a microcirculation frame for each of the mentioned instances. Since the thresholding algorithm is based on the histogram of the image, in case of excessive/ uneven lighting, the histogram is negatively affected by having little variations in the values of the intensity bins. In case of lack of camera zooming, the identification of objects through vessel enhancement algorithm gets complicated due to fuzzy edges of objects. In case of Saliva and air bubbles, artifacts in form of false vessels appear after preprocessing. From the 124 analyzed samples, 15 samples had such issues and no FCD values were calculated for them. It is expected that these issues are addressed during data collection through proper surface preparation and lighting.

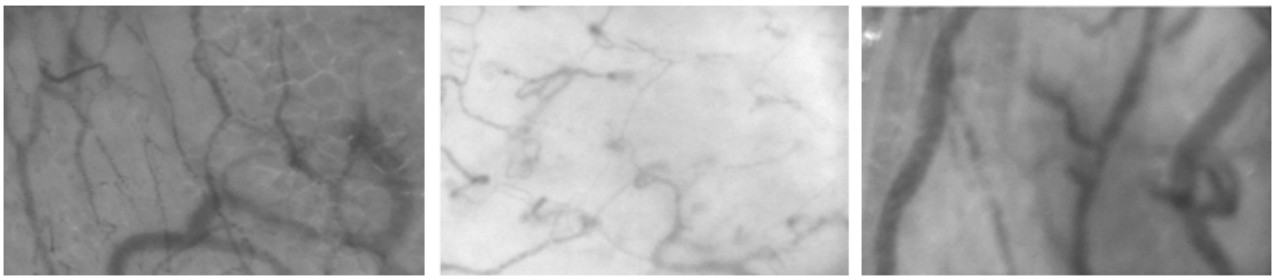

Figure 9.4: From left to right: presence of saliva, excessive lighting and lack of proper camera zooming in three microcirculation sample frames

The analysis of outliers of Bland-Altman plots of the algorithm indicates that some of

the outliers had one or two of the mentioned issues. The original video frame and the segmentation results for two of the outliers are shown in Figure 9.6. From top to bottom, the median of Heavily-Edited FCD for the frames are 20.86 and 21.53 and the algorithm FCD results are 9.43 and 12.75 respectively.

(d) The comparison of the FCD results calculated by the algorithm and those of Heavily-Edited AVA through analysis of multiple Bland-Altman plots shows the potentials of the algorithm in automating the analysis. AVA is a semi-automated software that allows for human interaction to adjust the vessel extraction parameters. When used without human interaction, AVA usually generates unreliable results. Figure 9.5 presents a visual representation of the segmentation result of the algorithm and that of Unedited AVA of a video frame. According to medical experts, the segmentation results of the algorithm are superior to that of unedited AVA. Unedited AVA segmentation result in Figure 9.5 erroneously catches part of the background and large blood vessels as capillaries and small blood vessels. This is further supported by the Bland-Altman comparison between the results of Heavily-Edited AVA and Unedited AVA.

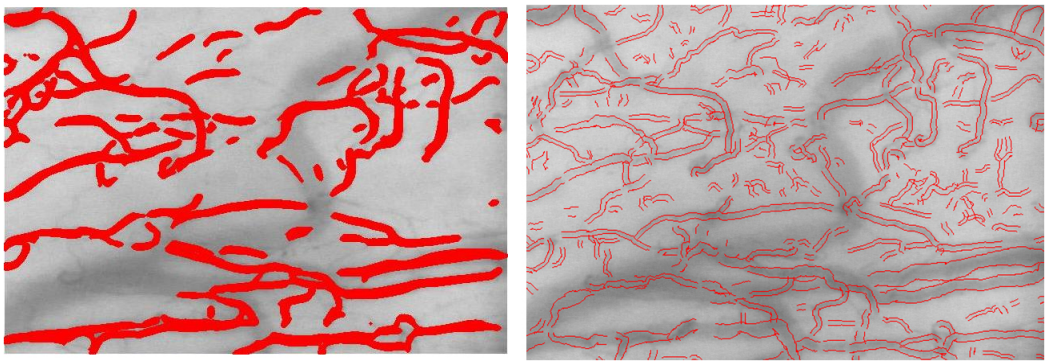

Figure 9.5: From left to right: algorithm segmentation result and Unedited AVA segmentation result of a microcirculation frame

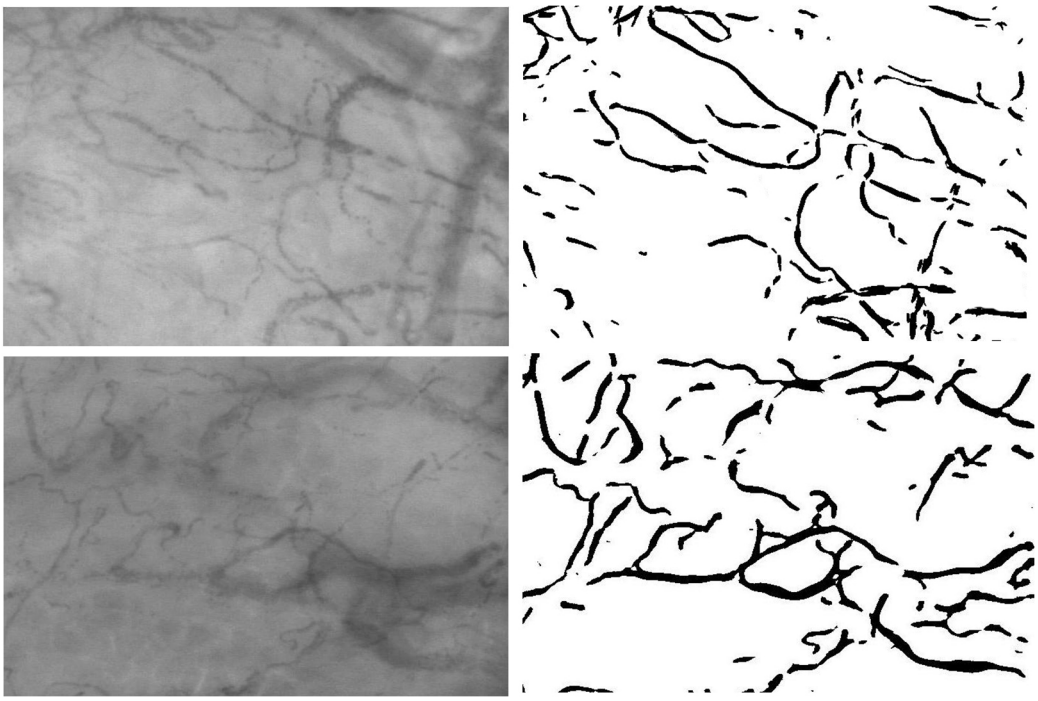

Figure 9.6: From left to right: original frame and segmentation result for two sample frames

9.2 Conclusion

The hierarchical algorithm introduces an effective method for segmentation of microcirculation videos. The conclusion drawn from applying the proposed algorithm to 97 human subjects and 12 swine subjects is as follows:

(a) The algorithm begins with registering the videos. Following that, the video enhancement step improves the visual quality of the video frames through preprocessing, vesselness filter and edge enhancement. While preprocessing reduces the effect of noise in the frames and enhances the contrast between blood vessels and background, the vesselness filter determines a framework for defining vessel objects in the frame. The method is an improved variation of an earlier method which reduces the amount of background noise that might be detected as vessels. Edge enhancement is a further step to improve the visualization of the tiny capillary edges. The frames are effectively combined through a variation of median filter that brings a bias factor, Shift Index, into account. Shift Index is effectively adjusted for each set of data. A threshold value is calculated using an entropic thresholding technique which is a variation of an earlier technique and considers flow information in the video frames in the calculation of threshold value. Finally, post-processing improves the segmentation results and leads to the calculation of FCD.

(b) The analysis of FCD results through Bland-Altman plots shows "Good Agreement" between the results of the algorithm and those of Heavily-Edited AVA. The algorithm is capable of calculating relatively accurate results automatically and can eliminate a large amount of manual work and system/ expert interaction.

(c) Having been tested on a small dataset, the algorithm has shown a potential capability to

distinguish between healthy and hemorrhaged swine subjects. Further testing requires a larger dataset of this type.

Chapter 10

Future Work

Having shown promising results, the proposed work can be further developed by focusing on the following areas:

(a) Some video samples used for this study were taken from healthy and hemorrhaged swine subjects. Use of a larger dataset with samples categorized by different disease types would be effective for further development of the technique, so to distinguish between disease types based on microcirculatory measures (e.g. FCD).

(b) Automated calculation of the velocity of blood flow in capillaries and small blood vessels may add value to the quantitative assessment of microcirculation videos. The current method can be extended by adding a velocity measurement technique.

(c) The only microcirculation measure calculated in this research is FCD. Additional quantitative measures suggested in microcirculation studies include Microcirculatory Flow Index (MFI) and Proportion of Perfused Vessels (PPV). MFI divides the blood flow into different levels (e.g. no flow, intermittent, sluggish and normal) and PPV is the ratio of number of blood vessels with flow to the total number of blood vessels. Calculating MFI and PPV may allow for further analysis of microcirculation videos.

(d) The algorithm may have limitations in accurate detection of capillaries and blood vessels in presence of saliva/ air bubbles, excessive/uneven lighting and lack of proper camera zooming. Furthermore, as can be seen in Figure 8.1, some of thick blood vessels appear as two parallel thin vessels as a result of edge enhancement stage and some of blood vessels are not well-connected as a result of insufficient region growing. The mentioned issues need to be addressed as part of the future work.

Bibliography

[1] A Sinha and D Vaghela. Pulse oximetry and laser doppler flowmetry for diagnosis of pulpal vitality. *Journal of Interdisciplinary Dentistry*, 1(1):14–21, 2011.

[2] PE Spronk, C Ince, MJ Gardien, KR Mathura, HM Oudemans-van Straaten, and DF Zandstra. Nitroglycerin in septic shock after intravascular volume resuscitation. *Lancet*, 360:1395–1396, 2002.

[3] C Ince. The microcirculation is the motor of sepsis. *Critical Care*, 9(sppl 4):S13–S19, 2005.

[4] RM Bateman, MD Sharpe, and CG Ellis. Bench-to-bedside review: microvascular dysfunction in sepsis: hemodynamics, oxygen transport and nitric oxide. *Crit Care Med*, 7:359–373, 2003.

[5] RP Hebbel, R Osarogiagbon, and D Kaul. The endothelial biology of sickle cell disease; inflammation and chronic vasculopathy. *Microcirculation*, 11:129–151, 2004.

[6] MJ Stuart and RL Nagel. Sickle cell disease. *The Lancent*, 364:1343–1360, 2004.

[7] BI Levy, G Ambrosio, AR Pries, and HA Struijker-Boudier. Microcirculation in hypertension: a new target for treatment? *Circulation*, 104:735–740, 2001.

[8] C Verdant and D De Backer. Monitoring of the microcirculation may help us at the bedside. *Curr Opin Crit Care*, 11(3):240–244, 2005.

[9] Alam HB. Advances in resuscitation strategies. *International Journal of Surgery*, 9:5–12, 2011.

[10] M Fries, MH Weil, Y Chang, C Castillo, and W Tang. Microcirculation during cardiac arrest and resuscitation. *Critical Care Medicine*, 34:454–457, 2006.

[11] S Czernichow and T Ninomiya. Medicine to lower blood pressure significantly decreases risk for cardiovascular disease, stroke. Website, March 2010. http://www.newsroom.heart.org/index.php?s=43/item=981.

[12] L Kobayashia, D Lindquista, and I Jenouri. Comparison of sudden cardiac arrest resuscitation performance data obtained from in-hospital incident chart review and in situ high-fidelity medical simulation. *Resuscitation*, 81(4):463–471, 2010.

[13] DC Angus, WT Linde-Zwirble, J Lidicker, G Clermont, J Carcillo, and MR Pinsky. Epidemiology of severe sepsis in the united states: analysis of incidence, outcome and associated costs of care. *Critical Care Medicine*, 29(7):1303–10, 2001.

[14] DC Brousseau, JA Panepinto, M Nimmer, and RG Hoffmann. The number of people with sickle-cell disease in the united states: national and state estimates. *Am J Hematol*, 85(1):77–78, 2010.

[15] Division of News Office of the Associate Director for Communication and Electronic Media. May is high blood pressure education month. Website, May 2011. http://www.cdc.gov/features/highbloodpressure/.

[16] D De Backer, S Hollenberg, C Boerma, P Goedhart, G Büchele, G Ospina-Tascon, I Dobbe, and C Ince. How to evaluate the microcirculation: report of a round table conference. *Crit Care*, 11(5):R101, 2007.

[17] RF Tuma, WN Duran, and K Ley. *Handbook of Physiology Microcirculation.* Elsevier Science, 2008.

[18] BD Spiess. Critical oxygen delivery: the crux of bypass with a special look at the microcirculation. *Extra-Corporeal Technology*, 364:10–6, 2011.

[19] GE Nilsson, T Tenland, and PA Oberg. Evaluation of a laser doppler flowmeter for measurement of tissue blood flow. *Biomedical Engineering, IEEE Transactions on*, BME-27(10):597 –604, 1980.

[20] O Genzel-Boroviczeny, J Strotgen, AG Harris, K Messmer, and F Christ. Orthogonal polarization spectral imaging (ops): A novel method to measure the microcirculation in term and preterm infants transcutaneously. *Pediatr Res*, 51:386–391, 2002.

[21] PT Goedhart, M Khalilzada, R Bezemer, J Merza, and C Ince. Sidestream dark field (sdf) imaging: a novel stroboscopic led ring-based imaging modality for clinical assessment of the microcirculation. *Opt Express*, 15:15101–15114, 2007.

[22] PE Spronk, DF Zandstra, and C Ince. Bench-to-bedside review: sepsis is a disease of the microcirculation. *Crit Care*, 8:462468, 2004.

[23] JJ Staal, MD Abramoff, M Niemeijer, MA Viergever, and B van Ginneken. Ridge based vessel segmentation in color images of the retina. *IEEE Transactions on Medical Imaging*, 23:501–509, 2004.

[24] A Hoover, V Kouznetsova, and M Goldbaum. Locating blood vessels in retinal images by piece-wise threhsold probing of a matched filter response. *IEEE transactions on medical imaging*, 19:203–210, 2000.

[25] KA Vermeer, FM Vos, HG Lemij, and AM Vossepoel. A model based method for retinal blood vessel detection. *Computers in Biology and Medicine*, 34:209219, 2004.

[26] U Rost, H Munkel, and CE Liedtke. A knowledge based system for the configuration of image processing algorithms. *Fachtagung Informations und Mikrosystem Technik*, 1998.

[27] H Chen and J Hale. An algorithm for mr angiography image enhancement. *Magn Res Med*, 33:534–540, 1995.

[28] YP Du and DL Parker. Vessel enhancement filtering in three-dimensional mr angiograms using long-range signal correlation. *J Magn Reson Imaging*, 7:447–450, 1997.

[29] S Aylward, E Bullit, S Pizer, and D Eberly. Intensity ridge and widths for tubular object segmentation and description. *Math Meth Biomed Imag Anal*, pages 131–138, 1996.

[30] Th Koller, G Gerig, G Szekely, and D Dettwiller. Multiscale detection of curvilinear structures in 2-d and 3-d image data. *Eur Conf Comp Vision, IEEE Computer Society Press*, pages 864–869, 1995.

[31] C Lorenz, IC Carlsen, TM Buzug, C Fassnacht, and J Weese. Multi-scale line segmentation with automatic estimation of width, contrast and tangential direction in 2d and 3d medical images. *Lect Notes Comp Science, Springer-Verlag, Berlin*, pages 233–242, 1997.

[32] Y Sato, S Nakajima, H Atsumi, Th Koller, G Gerig, S Yoshida, and R Kikinis. 3d multi-scale line filter for segmentation and visualization of curvilinear structures in medical images. *Lect Notes Comp Science, Springer-Verlag, Berlin*, pages 213–222, 1997.

[33] AF Frangi, WJ Niessen, KL Vincken, and MA Viergever. Multiscale vessel enhancement filtering. *n Lecture Notes in Computer Science. Berlin, Germany: Springer-Verlag*,

1496:130–137, 1998.

[34] R Manniesing, MA Viergever, and Niessen WJ. Vessel enhancing diffusion a scale space representation of vessel structures. *Medical Image Analysis*, 10:815825, 2006.

[35] K Krissian. Flux-based anisotropic diffusion applied to enhancement of 3-d angiogram. *IEEE Transaction on Medical Imaging*, 21(11):14401442, 2002.

[36] Radeva P Canero, C. Flux-based anisotropic diffusion applied to enhancement of 3-d angiogram. *Pattern Recognition Letters*, 24:31413151, 2003.

[37] S Chaudhuri, S Chatterjee, N Katz, M Nelson, and M Goldbaum. Detection of blood vessels in retinal images using two-dimensional matched filters. *IEEE Trans Med Imag*, 8:2639, 1989.

[38] LB Becker, ML Weisfeldt, MH Weil, T Budinger, J Carrico, K Kern, G Nichol, I Shechter, R Traystman, C Webb, H Wiedemann, R Wise, and G Sopko. The pulse initiative: scientific priorities and strategic planning for resuscitation research and life saving therapies. *Circulation*, 105(21):1562–2570, 2002.

[39] L Xu and X Lin. Digital image stabilization based on circular block matching. In *IEEE Trans. Consum. Electron.*, volume 52-2, page 566574, 2006.

[40] SJ Ko, SH Lee, and KH Lee. Digital image stabilizing algorithms based on bit-plane matching. *IEEE Transactions on Consumer Electronics*, 44:617–622, 1998.

[41] S Erturk. Digital image stabilization with sub-image phase correlation based global motion estimation. *IEEE transactions on consumer electronics*, 49:1320, 2003.

[42] Lim JS. *Two-Dimensional Signal and Image Processing*. Prentice-Hall, 1990.

[43] J Jin, Z Zhu, and G Xu. Digital video sequence stabilization based on 2-d motion estimation and inertial motion filtering. *Real-Time Imaging*, 7:357–365, 2001.

[44] J Chang, W Hu, M Cheng, and B Chang. Digital image translational and rotational motion stabilization using optical flow technique. *IEEE Transactions on Consumer Electronics*, 48-1:108–115, 2002.

[45] A Crawford, H Denman, F Kelly, F Pitie, and A Kokaram. Gradient based dominant motion estimation with integral projections for real time video stabilization. In *International Conference on Image Processing*, volume 5, page 3371 3374, 2004.

[46] C Erdem and A Erdem. An illumination invariant algorithm for subpixel accuracy image stabilization and its effect on mpeg-2 video compression. *Elsevier Signal Processing: Image Communication*, 16:837–857, 2001.

[47] J Bergen, P Anandan, K Hanna, and R Hingorani. Hierarchical model-based motion estimation. 588:237–252, 1992.

[48] SG Chang, Y Bin, and M Vetterli. Spatially adaptive wavelet thresholding with context modeling for image denoising. *Image Processing, IEEE Transactions*, 9:1522 – 1531, 2000.

[49] JB Zimmerman, SB Cousins, KM Hartzell, ME Frisse, and MG Kahn. A psychophysical comparison of two methods for adaptive histogram equalization. *J Digit Imaging.*, 1:82–91, 1989.

[50] K Zuiderveld. Contrast limited adaptive histogram equalization. *Graphics gems IV*, pages 474–485, 1994.

[51] J Sijbers, AJ Dekker, JV Audekerke, M Verhoye, and D Van Dyck. Estimation of the noise in magnitude mr images. *Magnetic Resonance Imaging*, 16:8790, 1998.

[52] M Martnez-Prez, A Hughes, A Stanton, S Thom, A Bharath, and K Parker. Retinal blood vessel segmentation by means of scale-space analysis and region growing. 1679:90–97, 1999.

[53] N Otsu. A threshold selection method from gray-level histograms. *IEEE Transactions On Systems, Man, And Cybernetic*, 9:62–66, 1979.

[54] SK Hanneman. Design, analysis and interpretation of method-comparison studies. *AACN Adv Critical Care*, 19(2):223234, 2008.

[55] JM Bland and DG Altman. Statistical methods for assessing agreement between two methods of clinical measurement. *Lancent*, 327:307–310, 1986.

Appendix A

FCD Table

This chapter contains the table for of values calculated for 97 human subjects. The FCD values were used to calculate the values needed for Bland-Altman plots. In the tables the first column presents the FCD values calculated by the algorithm, the second column shows the median of Heavily-Edited Produced FCD by experts, the third column presents the mean of Heavily-Edited Produced FCD by experts, the fourth column shows Heavily-Edited Produced FCD by expert A (one of the experts), and the fifth column presents Heavily-Edited Produced FCD by expert B (another experts).

	Algorithm	Median by AVA	Mean by AVA	AVA (Expert A)	AVA (Expert B)
Data 1	7.31	4.56	4.36	1.27	7.07
Data 2	8.51	9.68	9.42	8.10	10.47
Data 3	9.40	10.40	10.08	6.46	13.37
Data 4	9.43	20.52	19.80	18.01	20.86
Data 5	10.20	14.82	16.58	14.55	20.36
Data 6	10.23	11.56	11.70	10.60	12.86
Data 7	10.50	10.31	10.03	7.44	12.35
Data 8	11.21	9.93	10.19	9.25	11.40
Data 9	11.23	8.92	9.16	8.57	10.21
Data 10	11.61	10.13	11.77	9.72	15.46
Data 11	11.71	12.87	13.29	12.33	14.66
Data 12	11.78	10.04	10.35	8.23	12.79
Data 13	11.92	11.72	11.73	11.14	12.33
Data 14	12.01	11.31	11.20	10.81	11.47
Data 15	12.03	11.45	11.66	10.40	13.57
Data 16	12.43	12.84	13.16	12.58	14.07
Data 17	12.56	13.89	14.18	13.41	15.23
Data 18	12.68	18.79	18.70	16.87	20.16
Data 19	12.68	16.82	17.22	16.77	18.07
Data 20	12.75	21.53	21.56	21.24	21.92
Data 21	12.85	13.31	13.42	12.85	14.11
Data 22	12.85	12.94	13.13	12.56	13.96
Data 23	12.88	12.27	12.35	11.86	12.93
Data 24	12.89	13.53	14.36	12.77	16.79
Data 25	12.93	18.31	18.25	18.10	18.34
Data 26	13.09	13.41	13.47	12.66	14.35
Data 27	13.14	13.42	14.20	12.40	16.77
Data 28	13.25	14.28	13.88	11.84	15.53
Data 29	13.46	13.50	14.00	13.34	15.75
Data 30	13.64	13.86	13.85	13.56	14.12
Data 31	13.66	12.94	12.28	9.62	14.28
Data 32	13.83	13.57	13.67	13.32	14.13
Data 33	14.02	14.40	13.91	12.64	14.69
Data 34	14.11	16.98	17.07	16.19	17.80
Data 35	14.27	13.02	13.91	12.97	15.75
Data 36	14.37	13.13	12.35	10.36	13.56
Data 37	14.47	14.01	14.16	13.67	14.79
Data 38	14.47	11.74	11.60	9.56	13.07
Data 39	14.47	14.25	14.58	13.11	16.62
Data 40	14.50	15.38	15.40	14.12	16.72
Data 41	14.63	16.89	16.55	15.49	17.28
Data 42	14.69	14.92	14.92	14.29	15.54
Data 43	14.76	16.40	15.07	11.70	17.10
Data 44	14.77	14.53	14.25	13.07	15.16
Data 45	14.82	18.02	18.10	17.25	19.02

	Algorithm	Median by AVA	Mean by AVA	AVA (Expert A)	AVA (Expert B)
Data 46	14.82	15.47	14.66	13.20	15.68
Data 47	14.88	14.14	14.16	13.05	15.29
Data 48	14.90	15.67	15.12	14.01	15.68
Data 49	14.94	13.95	13.54	10.75	15.91
Data 50	14.96	11.15	11.69	9.36	15.07
Data 51	14.96	19.26	17.20	12.55	19.80
Data 52	14.97	13.16	13.56	11.12	16.32
Data 53	15.01	13.90	14.17	13.05	15.56
Data 54	15.03	16.28	15.89	14.89	16.49
Data 55	15.11	15.72	15.52	14.84	16.01
Data 56	15.26	15.90	15.85	15.54	16.11
Data 57	15.33	15.86	16.13	15.86	16.67
Data 58	15.36	16.96	16.72	15.71	17.49
Data 59	15.41	15.72	15.76	15.36	16.21
Data 60	15.41	15.36	14.47	12.60	15.62
Data 61	15.49	13.40	13.57	13.06	14.24
Data 62	15.58	14.69	14.31	13.05	15.18
Data 63	15.60	14.24	14.93	13.83	16.72
Data 64	15.61	18.17	18.26	17.66	18.95
Data 65	15.66	15.58	15.52	14.68	16.30
Data 66	15.82	16.28	16.14	14.47	18.37
Data 67	15.88	15.27	15.47	14.29	16.85
Data 68	15.90	15.39	15.89	14.88	17.40
Data 69	15.93	15.48	15.70	15.32	16.31
Data 70	16.05	21.53	21.98	21.17	23.88
Data 71	16.14	19.52	19.45	17.68	21.14
Data 72	16.29	14.95	15.23	13.53	17.22
Data 73	16.45	15.91	15.74	14.39	16.99
Data 74	16.51	15.92	16.65	15.85	18.19
Data 75	16.55	16.99	17.08	16.57	17.68
Data 76	16.64	19.41	18.47	15.63	19.79
Data 77	16.71	16.91	17.16	16.31	18.25
Data 78	16.81	16.31	16.17	13.91	17.90
Data 79	16.83	12.84	12.72	10.50	14.81
Data 80	17.00	16.62	16.66	15.39	18.55
Data 81	17.01	17.23	16.39	14.03	17.90
Data 82	17.08	19.68	19.80	18.82	20.90
Data 83	17.42	17.49	17.48	16.92	18.03
Data 84	17.49	16.22	16.08	15.27	16.86
Data 85	17.66	19.49	19.72	18.46	21.20
Data 86	17.72	18.51	18.18	16.36	19.03
Data 87	18.27	19.36	20.49	19.35	22.75
Data 88	18.47	21.62	21.41	19.23	23.03
Data 89	18.64	20.57	20.13	19.19	20.64
Data 90	18.73	16.63	11.13	16.63	16.77

	Algorithm	Median by AVA	Mean by AVA	AVA (Expert A)	AVA (Expert B)
Data 91	18.78	18.00	18.05	17.18	18.97
Data 92	18.78	18.22	18.10	15.74	20.33
Data 93	20.20	21.89	21.35	17.85	23.11
Data 94	20.20	16.24	15.97	14.75	16.72
Data 95	20.44	23.26	24.71	23.18	27.70
Data 96	20.68	20.43	19.99	17.59	21.96
Data 97	21.28	23.50	23.23	22.02	24.16

List of Publications:

N. Mirshahi, S. Demir, K. Ward, R. Hobson, K. Najarian, '*An Adaptive Entropic Thresholding Technique for Image Processing and Diagnostic Analysis of Microcirculation Videos*', The International Journal on Advances in Life Sciences, vol. 2, no. 3 and 4, year 2010,p 133-142

S. Vasilache, N. Mirshahi, S. Ji, J. Mottonen, D.J. Jacobs, K. Najarian, '*A Signal Processing Method to Explore Similarity in Protein Flexibility*', Advances in Bioinformatics, Volume 2010 (2010), Article ID 454671, 8 pages doi:10.1155/2010/454671

N. Mirshahi, S. Demir, K. Ward, R. Hobson, K. Najarian, '*A Multi-Resolution Entropic-based Image Processing Technique for Diagnostic Analysis of Microcirculation Videos*', The Second International Conference on Advances in Biotechnologies (BIOTECHNO 2010), Cancun, Mexico, March 7-13, 2010.

S. Demir, N. Mirshahi, K. Ward, R. Hobson, K. Najarian, '*Vessel Extraction of Microcirculatory Video Recordings Using Multi-Thresholding Based Verification Algorithm*', The Second International Conference on Advances in Biotechnologies (BIOTECHNO 2010), Cancun, Mexico, March 7-13, 2010.

S. Demir, N. Mirshahi, K. Ward, R. Hobson, K. Najarian, '*Vessel Segmentation Based on Multi-Thresholding for Diagnostic Analysis of Microcirculation*', Circulation. 2009;120:S1491.

S. Demir, N. Mirshahi, M. H. Tiba, G. Draucker, K. Ward, R. Hobson and K. Najarian, '*Image Processing and Machine Learning for Diagnostic Analysis of Microcirculation*', IEEE/ICME International Conference on Complex Engineering CME 2009, Phoenix, AZ, USA, April 2009.

VITA

Nazanin Mirshahi was born on August 2, 1982, in Mashhad, Iran and is an Iranian Citizen. In 2004, she received her Bachelor of Science in Software Engineering from Azad University, Computer Engineering Department, Mashhad, Iran. She also received an M.S. degree in Computer Science from Computer Science Department at VCU, Richmond, VA, USA in 2010 and an M.B.A. (with a concentration in Information Resource Management) from the School of Business VCU, Richmond, VA, USA in 2011. Her research interests include biomedical image and signal processing, and computer-aided decision support systems.

Work Experience:

Ph.D. Intern, Virginia Biosciences Commercialization Center, Richmond, VA, USA. (January 2011 - December 2011)

Graduate Assistant, School of the Arts, Virginia Commonwealth University, Richmond, VA, USA. (August 2010 - May 2011)

Graduate Research Assistant, Department of Computer Science, Virginia Commonwealth University, Richmond, VA, USA. (August 2008 - August 2010)

Application Developer Intern, Virginia Housing Development Authority, Richmond, VA, USA. (January 2008 - August 2008)

Awards:

Third Year Ph.D. Student Award of Computer Science Department at VCU, 2011

Best Paper Award of The Second International Conference on Advances in Biotechnologies (BIOTECHNO 2010), Cancun, Mexico, March 7-13, 2010.